Desalination 443 (2018) 27–43

Contents lists available at ScienceDirect

Desalination

journal homepage: www.elsevier.com/locate/desal

A robust model of brackish water electrodialysis desalination with experimental comparison at different size scales

Natasha C. Wright[*,1], Sahil R. Shah[*,1], Susan E. Amrose, Amos G. Winter V.

Department of Mechanical Engineering, Massachusetts Institute of Technology, Cambridge, MA 02139, USA

ARTICLE INFO

Keywords:
Electrodialysis
Brackish groundwater
Energetic model
Desalination model

ABSTRACT

This paper presents a robust analytical model for brackish water desalination using electrodialysis (ED), with prediction of the desalination rate, limiting current density, and total energy use including pumping energy. Several assumptions reduce computation time and accurately model ED system behavior. The predicted desalination rate, limiting current density, and total energy usage agree with measurements across two diverse ED stack designs, differing in total membrane area (0.18 m^2, 37.1 m^2), membrane manufacturers (GE Water, PCA GmbH), and flow channel spacers. The commercial-scale stack was additionally tested with real groundwater, demonstrating that brackish groundwater may be modeled as an equivalent concentration NaCl solution. Sensitivity to the membrane diffusion coefficient, area available for ion transport, level of discretization along the flow channel length, boundary layer and membrane resistances, and water transport are analyzed to guide empirical characterization when higher accuracy is required. No single existing model for pressure drop in the membrane spacers could accurately predict pumping power in both stacks. One model for each stack was found to reasonably approximate pressure drop, however experimental validation of specific spacer designs is recommended. The fully quantitative, parametric description of electrodialysis behavior presented forms a useful tool to design, evaluate, and optimize ED systems.

1. Introduction

This study presents and evaluates a model for electrodialysis (ED) desalination capable of predicting desalination rate, limiting current density, and total energy use including pumping energy. ED is a membrane-based desalination technology used to treat approximately 425,000 m^3 of brackish water (salinity < 3000 mg/L) daily [1]. While this accounts for only 6% of the total brackish water desalination capacity (86% is completed using reverse osmosis) [1], the growing demand for low cost, low energy-consuming, high-recovery brackish water desalination solutions has created a renewed interest in ED [2-7]. In addition, other applications of ED, such as desalination of dyes and removal of copper and nitrates, continue to be investigated [8-10].

There are several approaches to modeling ED systems that span from simple polynomial correlations [11] and analytic derivations [12,13] to computational fluid dynamics (CFD) simulations [14,15]. Simple correlations do not maintain fidelity over a broad range of system configurations while CFD solutions have a high computational cost. There is a need to predict desalination performance and pressure losses across the wide variety of ED systems used in water treatment using models that are less computationally intensive, in order to facilitate parametric design studies.

Several authors separately model the mass transfer [12,16], limiting current density [17-19], and pressure losses throughout the ED membrane stack [20-24]. However, few authors have united all of these aspects into a single model. A combined model is critical to develop a complete understanding of the behavior of an ED system. For example, while increased linear flow velocity (obtained by increased flow rate, thinner channels, or lower spacer void fractions) increases mass transfer rates and raises the limiting current density, it also increases the pressure drop over the stack, thereby increasing total energy consumption. Including these types of coupled interactions improves the accuracy of the model as well as its usefulness as a tool to design and optimize ED systems for performance, cost, and energy consumption.

Of the few models that do consider combined effects [3,4,13,16], all rely on empirically derived parameters that require experimental characterization of a specific ED system prior to use of the model. Here, we provide further experimental validation of their work, and present simplifying approximations that predict, with good accuracy, the performance of stack configurations that deviate from those tested by other

* Corresponding authors.
E-mail addresses: ncwright@mit.edu (N.C. Wright), sahils@mit.edu (S.R. Shah).
[1] Co-authors.

https://doi.org/10.1016/j.desal.2018.04.018
Received 20 November 2017; Received in revised form 2 April 2018; Accepted 17 April 2018
Available online 29 May 2018

authors.

In this paper, we present a model of ED to predict desalination rate, limiting current density, and energy consumption. We offer simplifying approximations to make the model easier to implement for simulation and design optimization purposes, and present the sensitivity of the model to those simplifications. We then compare model predictions and the measured performance for two diverse size scales and designs of ED stacks: a PCA GmbH 64 0 02 bench-scale stack (0.18 m^2 total membrane area), and a GE Water & Process Technologies commercial-scale stack (37.1 m^2 total membrane area). In both cases, we find good agreement with model predictions without explicitly deriving empirical parameters or conducting prior system characterization. The two stacks incorporate different membranes, flow channel geometries, and spacer thicknesses and porosity, thus demonstrating the model's flexibility. The commercial-scale stack configuration was tested in a laboratory setting with a pure NaCl feed water solution as the model assumes, as well as in a pilot water treatment plant in Chelluru, India using real groundwater. The model presented will be useful to engineers and designers tasked with evaluating the performance of an existing ED process, or sizing and optimizing new systems.

2. Model description

In the ED process, saline water is circulated through an electrodialysis stack (Fig. 1) which contains a series of alternating anion exchange membranes (AEM) and cation exchange membranes (CEM). When an electric potential difference is applied across the stack, anions are drawn towards the anode, and cations towards the cathode. AEMs only pass anions, while the CEMs only pass cations, therefore generating alternating channels of diluate and concentrate.

This section describes three interdependent models to predict the desalination rate and total energy consumption for the ED process described above. First, we use a circuit analogy to model the rate of ion transfer (in the form of current) as a function of the applied voltage and given diluate and concentrate concentrations, in Section 2.2. Next, Section 2.3 provides a mass transfer model to predict the concentration along the ED stack as a function of current and time. The current and concentration in the channels are interdependent, and therefore solved simultaneously. Lastly, Section 2.7 models the pressure drop over the ED stack as a function of geometric properties and the flow rate in the channels. While this third model can be solved independently, the desalination rate and maximum applied current depend on the flow rate through the system. In order to estimate the flow rate for a given stack-pump combination, or the pressure drop at a desired flow rate, and subsequently understand the resulting energetic and desalination rate repercussions, it is prudent to consider all three models simultaneously.

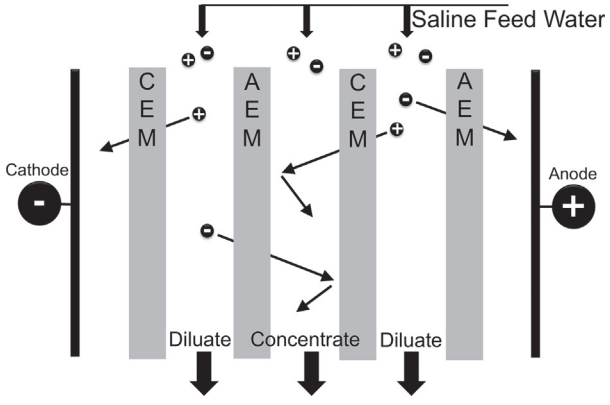

Fig. 1. Electrodialysis (ED) is the process of drawing ions out of a feed solution by applying an electric potential across a series of alternating anion (AEM) and cation (CEM) exchange membranes.

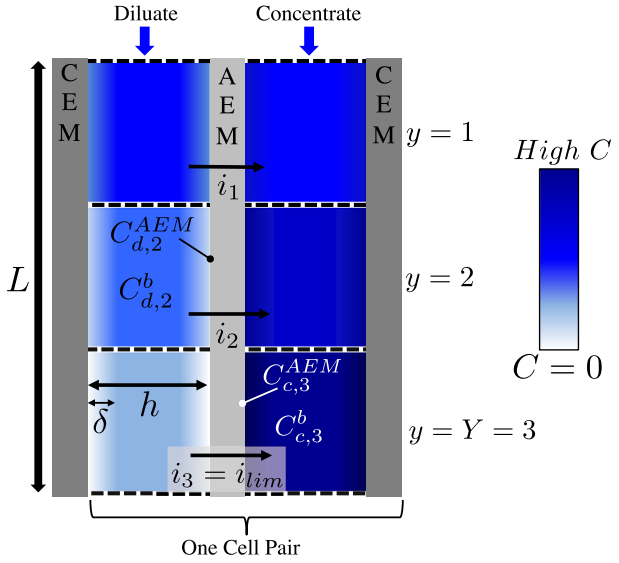

Fig. 2. Description of key dimensions and notation.

2.1. Variables and setup

We begin by considering the geometric and concentration variables for a single cell pair (Fig. 2). Molar concentration is denoted by C, where the superscript denotes the bulk, C^b, the AEM surface, C^{AEM}, or the CEM surface, C^{CEM}. The first subscript defines the concentration as being either in the diluate or concentrate channel (C_d, C_c respectively), and the second subscript denotes the lengthwise segment of the channel, y. The segment of the channel provides discretization for modeling purposes only; ED stacks are not physically segmented in this manner.

C_d decreases in the direction of flow until the final segment, $y = Y$. The opposite is true for C_c. Within any given segment (for example, $y = 2$), the volume is considered small enough such that both the bulk and membrane surface concentrations are assumed to be length-wise constant. When a voltage is applied, a concentration boundary layer of thickness δ extends from the membrane surfaces, where the concentration is $C^{AEM/CEM}_{d/c}$, to the bulk, where the concentration is $C^{b}_{d/c}$ (Fig. 2).

This model assumes that the same flow conditions exist in the diluate and concentrate channels. This is standard practice in commercial ED stacks to ensure that the pressure difference across the membranes is negligible and does not contribute to water transport. Both channels are the same dimensions and utilize the same turbulence-promoting spacer. This model assumes that the feed water contains a single 1:1 electrolyte. The extent to which it can be applied to solutions containing divalent ions is discussed in Section 5.7.

2.2. Circuit analogy and current calculation

The ED stack is modeled as an analogous DC circuit whereby the voltage applied at the electrodes (E_{total}), and the resulting current are related by

$$E_{\text{total}} = E_{\text{el}} + NE_{\text{mem},y} + Ni_y(R^b_{d,y} + R^b_{c,y} + R^{BL}_y + R^{AEM} + R^{CEM}), \quad (1)$$

where N is the number of cell pairs in the stack, and i_y is the per-segment current density (A/m^2). The area resistances $R^b_{d,y}$, $R^b_{c,y}$, R^{BL}_y, R^{AEM}, and R^{CEM} are associated with the bulk diluate and concentrate streams, the concentration boundary layers lumped together, and the exchange membranes (AEM, CEM), respectively (Ω m^2). Finally, E_{el} is the electrode potential difference and $E_{\text{mem},y}$ is the potential across each membrane-pair (V). The subscript y refers to the segment of the stack in all cases (Section 5.3 discusses discretization).

The total instantaneous current (I_{total}), assuming uniform segmentation, is the sum of all current densities (i_y), multiplied by the product of the segment length (L/Y), width (W), and the open-area porosity of the turbulence-promoting channel spacer (ϕ_A) as given in Eq. (2).

$$I_{total} = \phi_A \left(\frac{WL}{Y}\right) \sum_{y=1}^{Y} i_y \tag{2}$$

The area resistances in Eq. (1), and thus I_{total}, vary with concentration along the length of the stack, and may also vary with time for unsteady operation, as is the case for batch processes.

For desalination of pure sodium chloride, the reduction of hydrogen ions at the cathode and the oxidation of chloride ions at the anode maintain a standard cell potential of 1.4 V for the electrodes. The actual potential, which can be estimated using the Nernst equation, is dependent on temperature and ion concentration. For a standard ED stack, which typically contains more than 300 cell-pairs with each contributing ~1 V per cell pair, the electrode potential E_{el} is negligible. The remaining terms in Eq. (1) are evaluated in the following sections.

2.2.1. Area resistances

The area resistances of the bulk and boundary layers ($R^b_{d,y}$, $R^b_{c,y}$, R^{BL}_y) can be found by first calculating the equivalent conductance of the solution using an empirical relationship for the specific aqueous solution. The Onsager/Falkenhagen equation for 1-1 electrolytes (Eq. (3)) presents good agreement with experimental data for solutions up to 0.1 mol/L, and over a temperature range of 5–65° C [25]. Since we are specifically interested in modeling brackish water desalination, use of the Onsager/Falkenhagen equation is justified. The equivalent conductance at the concentration of interest is given by

$$\Lambda_C = \Lambda_0 - (B_1\Lambda_0 + B_2)\frac{\sqrt{C^*10^{-3}}}{1 + B_0 a\sqrt{C^*10^{-3}}}, \tag{3}$$

where C is the concentration of the solution (mol/m^3); a, B, B_1, and B_2 are unit-less empirically-determined coefficients dependent on the temperature of the solution (Table 1), and Λ_0 is the equivalent conductance at infinite dilution (temperature and electrolyte dependent, Scm^2/mol). For models in which the diluate channel concentration is above 0.1 mol/L, we recommend the review of conductivity models and their range of application prepared by De Diego et al. [26]. The resistivity, ρ (Ω m), of the solution at a concentration C is then

$$\rho = \frac{1}{\Lambda_C C}. \tag{4}$$

The dominant resistance in brackish water desalination using ED is the resistance of the diluate channels because resistivity increases sharply at low concentrations. Resistivity is also temperature dependent; the resistivity at 30°C is 20% less than at 20°C over the concentration range 0.5–50 mol/m^3. Therefore, groundwater temperature variation with location or time may produce non-negligible variation in resistivity.

Eqs. (3) and (4) are used to determine all diluate and concentrate stream resistances in

Table 1
Constants of the Onsager/Falkenhagen (Eq. (3)) for the equivalent conductance of electrolytes in water at various temperatures [25]. Λ_0 and a are for NaCl specifically, while all other parameters are valid for all 1-1 electrolytes.

	20°C	25°C	30°C	40°C
B_0	0.3276	0.3286	0.3297	0.3318
B_1	0.2269	0.2289	0.2311	0.2357
B_2	53.48	60.32	67.54	82.97
Λ_0	113.76	126.45	140.11	168.2
a(Å)	4	4	4	4

$$R^b_{d,y} = \rho^b_{d,y}(h - 2\delta), \tag{5}$$

$$R^b_{c,y} = \rho^b_{c,y}(h - 2\delta), \tag{6}$$

$$R^{BL}_y = R^{AEM}_{d,y} + R^{CEM}_{d,y} + R^{AEM}_{c,y} + R^{CEM}_{c,y}, \text{ and} \tag{7}$$

$$R^{AEM}_{d,y} = \frac{(\rho^b_{d,y} + \rho^{AEM}_{d,y})}{2}\delta. \tag{8}$$

All four boundary layer resistances in Eq. (7) are evaluated as shown in Eq. (8), which is specified for the diluate-AEM interface. The resistances are calculated using a mean concentration, and approximate resistivity as varying linearly over small concentration changes. Although the boundary layer resistance could be resolved more accurately, a linear approximation is sufficient because the contributions of the boundary layer resistances to the total resistance are small since δ is small with respect to the flow channel height (see Section 5.5).

Membrane resistances (R^{AEM}, R^{CEM}) are often provided by the manufacturer. However, these values are typically given at a single concentration while the effective membrane resistance is known to change with concentration of the solution contacting either side of the membrane [27]. The membrane resistance can be experimentally determined as a function of concentration. Here, we make the simplification that it is constant, provided that the diluate and concentrate concentrations being tested are near the concentration at which the membrane was characterized.

2.2.2. Membrane potential

The potential associated with the concentration difference across the exchange membranes ($E_{mem,y}$) is the sum of contributions from the AEM (E^{AEM}_y) and the CEM (E^{CEM}_y), given by

$$E^{AEM}_y = \frac{(2t^{AEM} - 1)RT}{F}\log\left(\frac{\gamma_c C^{AEM}_{c,y}}{\gamma_d C^{AEM}_{d,y}}\right), \text{ and} \tag{9}$$

$$E^{CEM}_y = \frac{(2t^{CEM} - 1)RT}{F}\log\left(\frac{\gamma_c C^{CEM}_{c,y}}{\gamma_d C^{CEM}_{d,y}}\right), \tag{10}$$

where R is the gas constant (J/mol-K), T is temperature (K), F is Faraday's constant (C/mol), and γ is the activity coefficient of the solution. t^{AEM} and t^{CEM} are the apparent transport numbers of the counterions (the anions in the AEM and cations in the CEM, respectively). These numbers account for the fraction of total current carried by the counterion across each respective membrane by migration. Measurements performed by McGovern et al. [28] for a cell-pair, $t^{AEM,CEM} = 0.96 \pm 0.04$ for concentrations below 10,000 mg/L. At ~7500 mg/L diluate, membrane manufacturers have reported transport numbers ranging from 0.90 (Membranes International) to > 0.96 (PCA GmbH). Therefore, at the low brackish water concentrations that are the focus of the present study (< 10,000 mg/L), it is reasonable to approximate both membranes as perfectly ion-selective, and assign counter-ion transport numbers of 1.

The activity coefficient γ depends on the solution's ionic strength and temperature. Data tables and theoretical expressions for a variety of electrolytes and concentration ranges can be found in Robinson and Stokes [29]. Extending the Debye-Hückel formula to fit measured activity coefficients (± 0.003) for NaCl over $1 \le C \le 2000$ mol/m^3 gives:

$$-\log\gamma = \frac{0.5065\sqrt{C^*10^{-3}}}{1 + 1.298\sqrt{C^*10^{-3}}} - 0.039(C^*10^{-3}). \tag{11}$$

While Eq. (11) will show that γ varies between 0.6 and 1.0 for most brackish water and seawater desalination processes, γ is set to 1.0 for the results shown in this paper due to its very small affect on the net applied voltage. Consider, for example, a batch process desalinating 3000 mg/L NaCl (γ = 0.819) to 150 mg/L (γ = 0.946) at 95% recovery

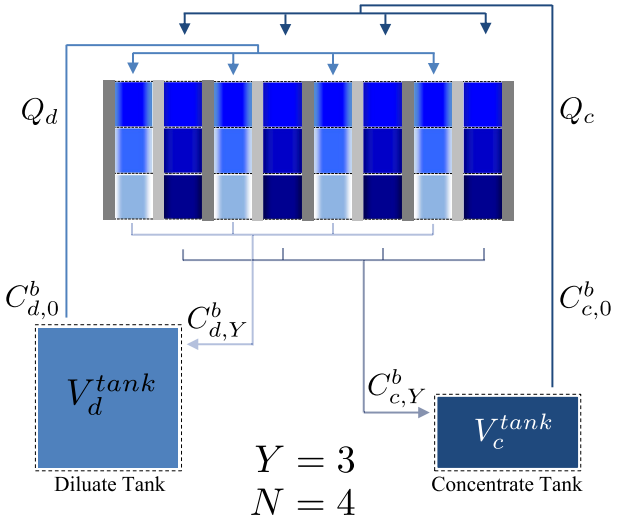

Fig. 3. Diagram of an ED system set up for batch desalination. Dashed black lines illustrate control boundaries used in mass balance Eqs. (12)–(15).

using 1 V per cell-pair, and producing 57,150 mg/L brine ($\gamma = 0.659$). Setting $\gamma = 1.0$ in this example decreases the predicted membrane potential by less than 10%, resulting in a total stack voltage under-prediction of < 1.1% over the entire duration of the batch. Given this low sensitivity, we make the simplification that $\gamma = 1$.

2.3. Mass transfer model

A mass balance is used to determine the concentration at any given time in the ED system. Fig. 3 shows a representative ED system arranged for batch desalination, comprising 4 cell pairs and showing 3 discretization units ($Y = 3$). The system contains the ED stack and two tanks through which the diluate and concentrate solutions are each continuously recirculated (the diluate through the diluate tank and the concentrate through the concentrate tank).

The rate of change of the concentration in the diluate and concentrate tanks is fully defined by the advective transport of ions (Eqs. (12) and (13)). Drawing a control volume (dashed lines in Fig. 3) about the tanks, we obtain that the mass balance for diluate tank is

$$\frac{dC^b_{d,0}}{dt} = \frac{1}{V_d^{\text{tank}}}[Q_d C^b_{d,Y} - Q_d C^b_{d,0}], \tag{12}$$

and the mass balance for concentrate tank is

$$\frac{dC^b_{c,0}}{dt} = \frac{1}{V_c^{\text{tank}}}[Q_c C^b_{c,Y} - Q_c C^b_{c,0}], \tag{13}$$

where $C^b_{d,0}$, $C^b_{c,0}$, $C^b_{d,Y}$, $C^b_{c,Y}$, are the concentrations of the diluate and concentrate streams at the inlet and outlet of the ED stack, Q_d, Q_c are the flow rates of the diluate and concentrate streams, and V_d^{tank}, V_c^{tank} are the volumes of water in the dilute and concentration tanks, respectively. In a continuous system, where the water is not recirculated, this tank mass-balance is not required. Instead, the feed concentration at the inlet to the stack is typically constant.

To determine the mass balance within the ED stack, Eqs. (14) and (15) are derived from the fundamental continuity equation and the Nernst-Planck equation which describes the motion of ions under the influence of advection, an ionic concentration gradient (resulting in diffusion) and an electric field (resulting in migration). For interested readers, the derivation from fundamental equations is provided by Lee [16]. For an individual segment within a channel, we obtain the mass balance for diluate cells as

$$\frac{dC^b_{d,y}}{dt} = \frac{1}{NV_y^{\text{cell}}}\left[Q_d(C^b_{d,y-1} - C^b_{d,y}) - \frac{N\phi I_y}{zF} + \frac{NA_y D^{AEM}(C^{AEM}_{c,y} - C^{AEM}_{d,y})}{l^{AEM}} + \frac{NA_y D^{CEM}(C^{CEM}_{c,y} - C^{CEM}_{d,y})}{l^{CEM}}\right], \tag{14}$$

and the mass balance for concentrate cells as

$$\frac{dC^b_{c,y}}{dt} = \frac{1}{NV_y^{\text{cell}}}\left[Q_c(C^b_{c,y-1} - C^b_{c,y}) + \frac{N\phi I_y}{zF} - \frac{NA_y D^{AEM}(C^{AEM}_{c,y} - C^{AEM}_{d,y})}{l^{AEM}} - \frac{NA_y D^{CEM}(C^{CEM}_{c,y} - C^{CEM}_{d,y})}{l^{CEM}}\right], \tag{15}$$

where N is the number of cell pairs, ϕ is the current leakage factor, I_y is the current in the discretized segment, z is the ion charge number, F is Faraday's constant, l^{AEM} and l^{CEM} are the thicknesses of the anion and cation exchange membranes, D^{AEM} and D^{CEM} are the diffusion coefficients of the solute in the AEMs and CEMs, and $C^{AEM}_{c,y}$, $C^{AEM}_{d,y}$, $C^{CEM}_{c,y}$, and $C^{CEM}_{c,y}$ are the concentrations of the diluate and concentrate streams at the interface with adjacent AEMs or CEMs in segment y. The current leakage factor ϕ accounts for the loss of current that occurs when an electrical path parallel to the active channel area exists for the current to flow through. Current leakage is a function of the stack construction and can be assumed negligible for a well-designed stack.

Within Eqs. (14) and (15), the first term represents advective transport of ions entering and exiting a segment, and the second term represents the migration of ions from diluate to concentrate compartment due to the electrical potential gradient, where the current I_y is found by solving Eqs. (1)– (10). The final two terms represent the back-diffusion of ions due to concentration differences that develop across each membrane. For batch operation, the concentration in the stack is changing with time through the desalination process; hence, the transient terms on the left of Eqs. (14) and (15) are non-zero. Conversely for a continuous system, steady-state operation can be modeled by setting these terms to zero.

2.3.1. Concentration at the membrane surfaces

Eqs. (7), (14) and (15) require the concentrations at the surfaces of the AEM and CEM exchange membranes in the diluate and concentrate channels. The surface concentration is obtained by balancing diffusion into the boundary layer with migration across the bounding membrane. For the four surface concentrations in the diluate and concentrate channels within a cell pair, this results in

$$C^{AEM}_{d,y} = C^b_{d,y} - \frac{\phi i_y (t^{AEM} - t_-)}{zFk}, \tag{16}$$

$$C^{CEM}_{d,y} = C^b_{d,y} - \frac{\phi i_y (t^{CEM} - t_+)}{zFk}, \tag{17}$$

$$C^{AEM}_{c,y} = C^b_{c,y} + \frac{\phi i_y (t^{AEM} - t_-)}{zFk}, \text{ and} \tag{18}$$

$$C^{CEM}_{c,y} = C^b_{c,y} + \frac{\phi i_y (t^{CEM} - t_+)}{zFk}, \tag{19}$$

where t_- and t_+ are transport numbers of the anions and cations in solution, respectively. For NaCl the transport number of the cations is $t_+ = 0.39$, while for the anions it is $t_- = 0.61$ (variation < 3% over a temperature range of 15–45° C and a concentration range of 0.0–0.1 mol/L) [30].

2.4. Water transport

Water transport through the membranes can occur due to osmosis and electro-osmosis (migration) such that the volume of the diluate tank in Eq. (12) decreases and the volume of the concentrate tank in Eq. (13) increases. We follow the work of Fidaleo and Moresi [13] to obtain the rate of change of volume (Eq. (20)), using values of L_w and t_w measured by McGovern [28]. Transport due to osmosis is given by

$$\frac{dV_c^{\text{tank}}}{dt} = N\left(\frac{LW}{Y}\right)M_{H_2O}\sum_{y=1}^{Y} L_w(\pi_{c,y} - \pi_{d,y}),$$
$$\text{where} \quad L_w = (1.6\times 10^{-3})(C_{c,y}^b)^{-0.416}. \tag{20}$$

Transport due to electro-osmosis is given by

$$\frac{dV_c^{\text{tank}}}{dt} = N\left(\frac{LW}{Y}\right)M_{H_2O}\sum_{y=1}^{Y} \frac{t_w i_y}{F},$$
$$\text{where} \quad t_w = (-1.37\times 10^{-7})(C_{c,y}^b)^2 - (1.099\times 10^{-3})C_{c,y}^b + 11.194. \tag{21}$$

In Eqs. (20) and (21), M_{H_2O} is the molar mass of water (kg/mol), L_w is the cell pair membrane water permeability (mol/bar-m^2-s), t_w is the dimensionless cell pair water transport number and $\pi_{c,y}$ and $\pi_{d,y}$ are the osmotic pressure of the concentrate and diluate, respectively (bar).

In brackish water desalination, recoveries are typically high such that larger volumes of diluate are produced compared to concentrate, and trans-membrane concentration differences are lower than in seawater desalination. As such, we do not expect water transport to have a significant effect on the modeled performance. We neglect water transport initially, and then discuss the effect of this assumption on model accuracy in Section 5.6.

2.5. Limiting current density

Due to the concentration boundary layer described in Section 2.1, there exists a maximum rate of ion transport that is bounded by the current density that results in a zero ion concentration at the membrane surface in the diluate channel. This phenomenon first occurs at the end of the flow path where the diluate concentration is the lowest ($y = Y$ in Fig. 2). The limiting current density i_{lim} (A/m^2) is estimated by setting the concentration at the AEM or CEM surface in Eqs. (16) and (17) to zero, resulting in

$$i_{lim}^{+,-} = \frac{C_d^b zFk}{t^{AEM,CEM} - t_{+,-}}, \tag{22}$$

where z is the valence of the ion, k (m/s) is the boundary-layer mass transfer coefficient, $t^{AEM,CEM}$ is the transport number of the counterion in the AEM or CEM membrane, and $t^{+,-}$ is the transport number of the cations or anions in the bulk solution, respectively, where its concentration is C_d^b. $t^{AEM,CEM}$ is assumed to be 1 in all cases per the discussion in Section 2.2.2. In the bulk solution, for a single 1-1 electrolyte, the limiting current is set by the lower of the two solution transport numbers. Because $t^+ < t^-$ (Section 2.3.1), $i_{lim} = i_{lim}^+$ throughout this investigation.

The boundary layer mass transfer coefficient k (m/s) depends on hydrodynamic factors, coupling the mass transfer and flow properties such that the design and operating parameters of an ED stack affect the pressure drop and subsequently, the final pump selection.

2.6. Coupling mass transfer to flow

By definition, the Sherwood number Sh, which is the ratio of advective to diffusive mass transport, is related to k by

$$k = \frac{ShD_{aq}}{d_h}, \tag{23}$$

where D_{aq} is the diffusion coefficient of the aqueous solution. For NaCl at 25°C, D_{aq} varies from 1.61×10^{-9} m^2/s at infinite dilution to 1.47×10^{-9} m^2/s at 0.5 mol/L [31]. Approximating D_{aq} as constant at 1.6×10^{-9} m^2/s (since brackish water desalination is being considered) produces less than 6% error in the boundary layer mass transfer coefficient k over the same concentration range. The hydraulic diameter d_h as defined by Pawlowski et al. [20] is

$$d_h = \frac{4\epsilon}{2/h + (1-\epsilon)(8/h)}, \tag{24}$$

where ϵ is the void fraction, defined later in Eq. (31). Mass transfer is then correlated to the flow properties via

$$Sh = 0.29Re_d^{0.5}Sc^{0.33}\,[32], \tag{25}$$

where the Schmidt number Sc is a material-dependent non-dimensional quantity relating the momentum and mass diffusivities, and the Reynolds number Re_d characterizes the flow. They are defined as

$$Sc = \frac{\mu}{\rho_{aq}D_{aq}}, \tag{26}$$

and

$$Re_d = \frac{\rho_{aq}u_{ch}d_h}{\mu}, \tag{27}$$

where ρ_{aq} is the density of the aqueous solution, μ is the viscosity of the solution, and the velocity in the spacer-filled channels is u_{ch} (Eq. (32)). From Eqs. (23)– (27), it is evident that a high linear flow velocity in the channels will produce an increase in the mass transfer coefficient and a corresponding increase in the limiting current density. In order to increase the desalination rate, a higher linear flow velocity is advantageous, however it will also increase pressure losses through the stack.

2.7. Pressure drop

This section reviews and compares four models for the pressure loss in the diluate and concentrate channels. We assume that channel losses are the dominant source of pressure loss, and test this assumption in Section 4.3.

2.7.1. Pressure drop model setup

Consider a flow channel with a mesh spacer, which is typically used in ED stacks to promote mass transfer. The variables defining the geometry of the spacer are given in Fig. 4. The spacer may be woven, as shown in the figure, or overlapped, where filaments running in one direction are always above filaments running in the other direction.

In all the following cases, the pressure drop model presented by the original authors will be translated to the Darcy-Weisbach equation for flow between two parallel flat plates, allowing straightforward comparison of friction factor predictions:

$$\Delta P = \frac{\rho_{aq}fLu_v^2}{4h}. \tag{28}$$

Here f is the Darcy friction coefficient, L is the length of the channel's active area (m), and h is the channel gap, assumed equal to the spacer thickness h_{sp} (m), unless otherwise noted. The void channel velocity u_v (m/s) (velocity with no spacer present) is related to the volumetric flow in each circuit Q by

$$u_v = \frac{Q}{WhN}, \tag{29}$$

where W is the width of the active area (m) and N is the number of cell-pairs. The standard definition of the Reynolds number Re for flow between two parallel flat plates is used, giving

$$Re = \frac{2\rho_{aq}u_v h}{\mu}. \tag{30}$$

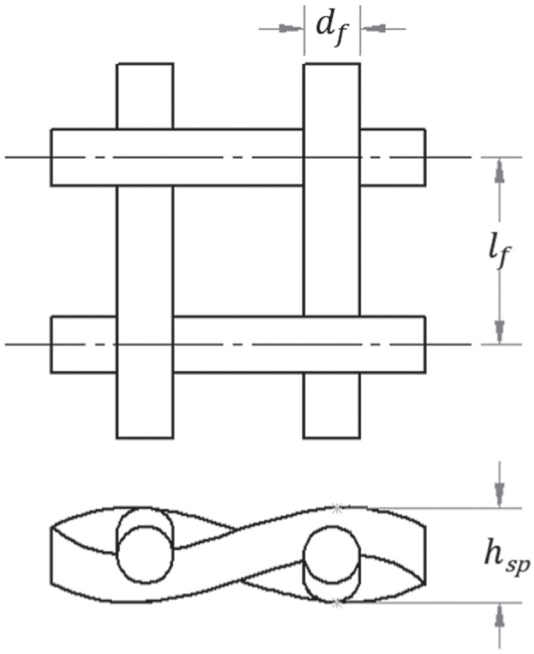

Fig. 4. A mesh spacer is often used as a turbulence promoter in the flow channels. The filaments in this spacer are woven rather than overlapped. The spacer thickness h_{sp} is equal to the channel gap h such that the spacer touches an AEM and CEM on either side.

The void fraction ϵ is the ratio of open volume to total volume in the spacer filled channel (Eq. (31)). It determines the actual flow velocity (Eq. (32)) in the channel and is important for both mass transfer and pressure drop calculations.

$$\epsilon = 1 - \frac{\pi d_f^2}{2 l_f h} \tag{31}$$

$$u_{ch} = \frac{Q}{\epsilon W h N} \tag{32}$$

The pressure drop (and associated friction factor f) is approximated by several authors through a series of CFD and/or experimental results. We present these models and compare their predictions against our experiments in Section 4.3.

2.7.2. Ponzio pressure drop model

Ponzio et al. investigated the relationship between friction factor and Re (Eq. (33)) for woven spacers in various orientations for Re of 2–2000 [22]. The transition out of creeping flow was modeled using CFD and observed experimentally. Using the data provided, and their observation that the friction factor scales with Re^{-1} for low Re and with $Re^{-0.37}$ for high Re, we derived the following relationship.

$$f = \frac{1400}{Re} \quad for \quad Re < 61$$
$$f = \frac{104.5}{Re^{0.37}} \quad for \quad Re \geq 61 \tag{33}$$

These results are limited to woven spacers where $l_f/h_{sp} = 2$ and $l_f/d_f = 4$. As the void fraction is a function of these two ratios alone (Eq. (31)), maintaining them as constant dictates that our predictions for pressure drop using Ponzio et al.'s model could only be calculated for a single void fraction of $\epsilon = 0.8$.

2.7.3. Pawlowski pressure drop model

The channel model implemented by Pawlowski et al. [20] is a modified version of the Darcy Weisbach equation for flow between two infinite parallel flat plates. It utilizes a modified channel hydraulic diameter that accounts for the void fraction (Eq. (24)) and the actual flow velocity u_{ch} rather than the void channel velocity u_v.

$$\Delta P = \frac{48 \mu L u_{ch}}{d_h^2} \tag{34}$$

The hydraulic diameter used here, and presented in Eq. (24), is a simplification of the relationship provided by Da Costa [33]. Pawlowski et al. assume that the thickness of the spacer h_{sp} is equal to the height of the channel h, and that the thickness of the spacer is exactly two times the diameter of the filament ($h_{sp} = 2d_f$). In reality, the filaments are slightly compacted against each other such that $h_{sp} < 2d_f$.

The following expression is Pawlowski et al.'s formulation translated into a friction factor that can be substituted into Eq. (28) for comparison to the correlations proposed by other authors:

$$f = \frac{24(2 + 8(1 - \epsilon))^2}{\epsilon^3 Re}. \tag{35}$$

Pawlowski et al. do not provide a range of Re or conditions over which this equation is expected to be valid.

2.7.4. Gurreri pressure drop model

Gurreri et al. [23] used CFD to investigate the pressure drop in the flow channel for both woven and overlapped spacers, with Reynolds numbers ranging from 1 to 64. The thickness of the spacer was assumed to be 1.8 times the diameter of the filament to account for the compaction that occurs where the filament strands cross. The geometries covered had l_f/h ratios of 2 ($\epsilon = 0.76$), 3 ($\epsilon = 0.84$), and 4 ($\epsilon = 0.88$). Translating Gurerri et al.'s results into a friction factor that can be substituted into Eq. (28) for comparison gives

$$f = 4\frac{40.37}{\epsilon^{5.35} Re} \tag{36}$$

for overlapped spacers, and

$$f = 4\frac{50.60}{\epsilon^{7.06} Re} \tag{37}$$

for woven spacers. Both friction factors are multiplied by 4 to convert from the Fanning friction factor used in Gurreri et al.'s paper to the Darcy friction factor used here. Note that we have applied a power law correlation on the void fraction to fit the data presented in Gurreri et al.'s work ($R^2 = 0.998$). However, their dataset contained only three data points and a linear fit ($R^2 = 0.990$) would have been equally appropriate. It is thus recommended that this correlation only be used within the range of void fractions investigated by Gurreri et al.

2.7.5. Kuroda pressure drop model

Finally, we consider a pressure drop correlation developed by Kuroda et al. [24]. Their experimental analysis considers four different mesh spacers. Unlike the models produced by Ponzio et al., Pawlowski et al., and Gurreri et al., where the spacer thickness h_{sp} is assumed to be equal to the channel thickness h, here the mesh thickness fills between 50 and 71% of the channel thickness. The experimentally determined correlation for the 0.5 mm thick spacer in a 1.0 mm channel has been used in recent ED models [4,34] and is given by

$$f = 4\frac{9.6}{\epsilon Re^{0.5}}. \tag{38}$$

Kuroda et al. also provide a correlation to connect all four tested spacers. In that correlation, $f = f(h^{0.5}, \epsilon^{-0.5}, l_f^{-0.57}, g^{-1})$, where g is the gap between the mesh spacer and the membrane (the channel wall) such that $g = h - h_{sp}$. Since this gap height is in the denominator of the fitting function, the correlation cannot be used directly for most ED stacks where $g = 0$. Using the same data set, we reformulated the correlation using the spacer thickness instead of the gap height, such that $f = f(h^{0.5}, \epsilon^{-0.5}, l_f^{-0.119}, h_{sp}^{-1})$. The resulting correlation for all four spacers is

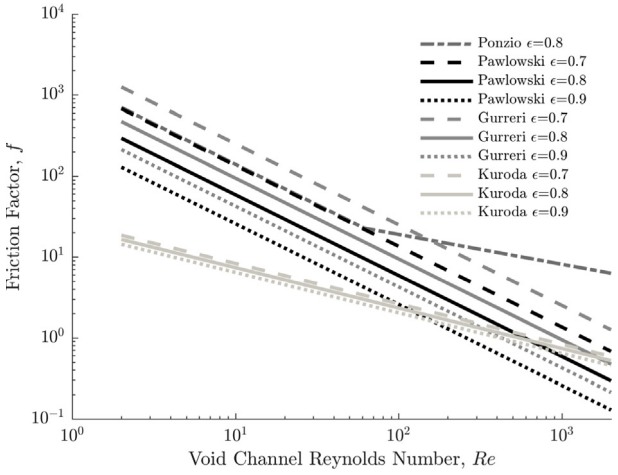

Fig. 5. Calculated friction factors from models by four different authors, used to predict the pressure drop in a spacer filled channel at void fractions of 0.7, 0.8, and 0.9. Kuroda et al. show less dependence on void fraction than the other models.

$$f = 4\frac{0.0557\sqrt{2h\epsilon}}{\epsilon Re^{0.5} l_f^{0.119} h_{sp}}, \tag{39}$$

where spacer dimensions must be given in meters [m]. Eq. (39) produces a maximum of 11% error compared to experiments by Kuroda et al. over $Re = 50-700$.

2.7.6. Comparison of model friction factors

Fig. 5 shows the relationship between the four friction factor correlations. Each correlation is shown at 3 different void fractions ($\epsilon = 0.7$, 0.8, and 0.9) except for Ponzio et al., which was only available for a single void fraction. All friction factors can be used directly in Eq. (28) to calculate pressure drop.

For the models proposed by Ponzio et al., Gurreri et al., and Pawlowski et al., the friction factor depends only on the void fraction and *Re*. The results vary by a factor of three for $Re < 100$ and the difference increases with increasing *Re*. This indicates that the pressure drop prediction could vary by a factor of three or more depending on the model used.

The friction factor developed from Kuroda et al.'s work (Eq. (39)) depends on the void fraction, *Re*, and spacer geometry. The result shown in Fig. 5 assumes $h = h_{sp} = 2d_f = 1$ mm. The filament pitch l_f can be calculated from these values and the void fraction (Eq. (31)). While the result shown in Fig. 5 is an order of magnitude lower than the other models at low *Re*, the correlation was developed using experimental results for $Re = 50-700$. At these higher *Re*, the result is on the same order as the other three models and matches the trend predicted by Ponzio et al. In Section 4.3, we evaluate all four models against experimental results.

2.8. Energy consumption

The total specific energy consumption, Γ_{total} (J/m^3) related to the ED process is the sum of the energy consumed for desalination and pumping,

$$\Gamma_{total} = \Gamma_{desal} + \Gamma_{pump}. \tag{40}$$

The specific energy associated with pumping a solution through each circuit of the ED stack is

$$\Gamma_{pump} = 2\frac{Q\Delta P}{\eta_{pump} Q_p}, \tag{41}$$

where η_{pump} is the efficiency of the pump, ΔP is the total pressure drop through the circuit, assumed equal for the diluate and concentrate sides if $Q = Q_d = Q_c$, and Q_p is the volumetric rate at which desalinated water is produced. Similarly, the energy consumed for desalination is

$$\Gamma_{desal} = \frac{E_{total} I_{total}}{Q_p}, \tag{42}$$

where recall that E_{total} is the total voltage applied to the stack. Since the current I_{total} in a batch system varies with time, Eq. (42) changes to

$$\Gamma_{desal} = \frac{1}{V_d^{tank}} \int_0^{t_{batch}} E_{total} I_{total} \, dt, \tag{43}$$

where t_{batch} is the batch duration for a diluate volume of V_d^{tank}.

3. Experimental setup and procedures

Model predictions for desalination rate, limiting current density, and pressure drop were evaluated using a bench-scale stack (0.18 m^2 total membrane area) and a commercial-scale test stack (37.1 m^2 total membrane area). The objective was to assess the accuracy of the model over a diverse range of geometries and common membrane and spacer types without explicitly deriving new empirical parameters or conducting prior system characterization. In this section, we describe the apparatus and procedures implemented for the validation exercise.

3.1. Bench-scale system

The bench scale system comprised a PCA GmbH 64-002, 14 cell pair ED stack of 8 cm × 8 cm active area ion exchange membranes sandwiched between two platinum coated titanium electrodes. Woven polypropylene spacers (thickness 0.35 mm) were placed between each membrane forming sheet-flow channels. Appropriate volumes of feed solution (± 0.025 L) were split between diluate and concentrate streams and recirculated through their respective channels and into separate magnetically stirred 1 L glass beakers using two KNF Flodos NF300 KPDC diaphragm pumps. The flow rates through the diluate and concentrate channels were controlled with two King Instrument 7430 Series glass tube flowmeters with valves (± 6%) over flow rates ranging between 0 and 1.7 L/min. A rinse solution was circulated at 2.5 ± 0.1 L/min through the electrode channel between the electrodes and the first CEM membrane on either side of the stack using a separate beaker and an Iwaki MD-20RZ centrifugal pump.

For desalination and limiting current tests, a Dr. Meter PS-305DM power supply was used to apply a constant voltage of (± 0.1 V) across the electrodes and record current (± 0.01 A). A Hach MP-4 meter was used to monitor diluate and concentrate conductivity (± 2%) at 1-min intervals. Batch desalination tests were terminated when the target conductivity, related to the target concentration in mg/L using Eq. (3), was achieved. Pressure drop through the concentrate and diluate circuits was measured using two Ashcroft 595-04 pressure gauges (± 3 kPa).

3.2. Commercial-scale system

The commercial-scale ED test stack comprised 56 cell pairs of 168 cm × 19.7 cm active area GE Water ion exchange membranes sandwiched between two platinum coated titanium electrodes. MkIV-2 type spacers (thickness 0.71 mm) were placed between each membrane, forming U-shaped channels. Appropriate volumes of feed solution (± 10 L) were split between diluate and concentrate streams and recirculated through their respective channels and into separate water tanks using two Flotec FP5172 pumps. Water leaving the diluate tank was divided between the diluate channels and the electrode rinse stream. A vertical pipe was inserted into both the diluate and concentrate tanks such that the solution leaving the stack would re-enter the tank in the middle of the volume to facilitate mixing and minimize concentration gradients within the tank. A Keysight N8760A DC power

supply was used to apply a constant voltage across the electrodes and measure current (± 0.1%).

Two Omega FP1406 flow meters and four Omega PX309 pressure gauges were used to monitor the flow rate (± 0.2 L/min) and pressure drop (± 2%) in the diluate and concentrate channels at the entry (flow and pressure) and exit (pressure) of the stack. Conductivity Instruments CDCE-90 in-line conductivity probes interfacing with CDCN-91 conductivity controllers were used to monitor conductivity (± 2%) immediately before entering and exiting the stack. Probes measuring the diluate conductivity ($C^b_{d,0}$ and $C^b_{d,Y}$) had cell constants of K = 1/cm and K = 0.1/cm, respectively. Probes measuring the concentrate conductivity ($C^b_{c,0}$ and $C^b_{c,Y}$) had cell constants of K = 10/cm. All sensors interfaced with National Instruments NI9203 or NI9205 data acquisition modules. The flow rate over each electrode was held at 5.7 ± 0.2 L/min, while the flow in the diluate channels varied with each experiment.

Batch desalination tests were terminated when the target conductivity, related to the target concentration in mg/L using Eq. (3), was achieved. All measured values were sampled at 1 Hz, and Q_d and Q_c were maintained at the same flow rate. For the pressure drop experiments, the flow rate was varied between 0 and 40 L/min using a butterfly valve upstream of the flow and pressure sensors.

3.3. Membrane and spacer properties

Values for all stack and global parameters used as model inputs are given in Tables 2 and 3. All membrane properties were taken from manufacturer data sheets [35-37], with the exception of the membrane resistances for the bench-scale stack since the solution concentration at which the membranes were tested was not provided, and the diffusion coefficients. Therefore, we used resistance values which were experimentally determined at brackish water concentrations by Ortiz et al. [12], for different ion exchange membranes (Neosepta, Tokuyama), which were however of similar thickness and polymeric form to those used in this study. Likewise, membrane diffusion coefficients, were taken from the experimental work of Amang et al., which were also derived for Neosepta membranes. Spacer thicknesses were measured using a caliper (± 0.01 mm) and area porosity was measured using a scaled photograph of the spacer mesh weave. The volume of the mesh was found by displacing water in a graduated cylinder (± 0.05 mL), from which the void fraction could be calculated. Photos of both experimental stacks are shown in Fig. 6.

The number of channel segments Y was selected by running simulations with an increasing number of segments until the value of the predicted current changed by less than 2% with the addition of another segment. Model predictions for the commercial-scale stack utilized a 10-segment discretization, a result further explored in Section 5.3.

Table 2
Stack parameters.

	Lab	Commercial
Stack properties		
Supplier	PCA GmbH	GE Water
Model	64-002	MkIV-2
Number of cell pairs	14	56
Membrane properties		
AEM model	PC-SA	AR204SZRA
CEM model	PC-SK	CR67HMR
Flow path width (cm)	8	19.7
Flow path length (cm)	8	168
AEM resistance (Ω cm^2)	29	7
CEM resistance (Ω cm^2)	24	10
Spacer properties		
Void fraction	0.60 ± 0.04	0.83 ± 0.03
Area porosity	0.62 ± 0.04	0.70 ± 0.02
Spacer thickness (mm)	0.35 ± 0.01	0.71 ± 0.01

Table 3
Global modeling parameters.

Parameter	Value	Ref
F (C/mol)	96,485	
D^{AEM} (m^2/s)	3.28×10^{-11}	[38]
D^{CEM} (m^2/s)	3.28×10^{-11}	[38]
D_{aq} (m^2/s)	1.6×10^{-9}	[31]
t_+	0.39	[30]
t_-	0.61	[30]
z	1	
ϕ	1	

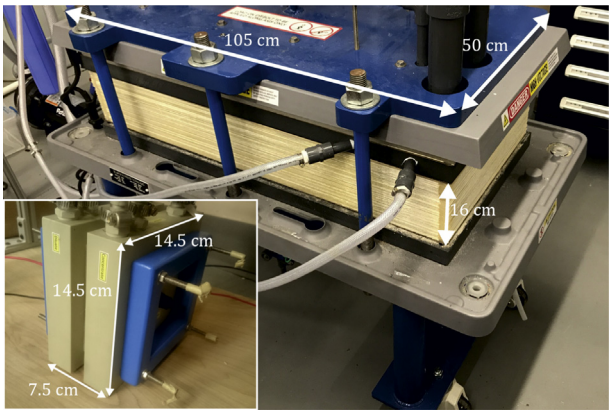

Fig. 6. Photos of the commercial-scale and bench-scale (lower left) ED stacks used in Tests A–F (Table 4) with overall stack dimensions for sense of scale.

3.4. Feed and rinse solutions

Feed and rinse solutions for the bench-scale stack were prepared using deionized water and the appropriate amount of reagent grade NaCl or Na_2SO_4 (0.2 M ± 3%). Feed solutions for the commercial-scale stack (also used for rinse streams) were prepared by adding reagent grade NaCl to Cambridge city tap water (Massachusetts, USA) in place of deionized water due to the large volume needed. In the year prior to testing (January–December 2016) Cambridge city tap water contained a maximum TDS level of 370 mg/L, approximately 86% of which comprised Na^+ and Cl^- ions. We thus approximate the prepared solution as pure NaCl. The total feed volume was prepared at once, recirculating for 30 min at a flow rate of 30 L/min to ensure mixing. The solution was then separated into the diluate and concentrate tanks at the start of each test.

3.5. Limiting current density experiments

The limiting current was measured following a common procedure outlined by other authors [17-19]. The current was measured for 0–100 V in increments of 4 V (for the bench-scale stack) or 2 V (for the commercial-scale stack) while circulating a solution of constant concentration through both the diluate and concentrate channels at three different flow rates. The resulting current vs. voltage plot can be divided into two regions which are differentiated by slope: a region under-limiting current and a region over-limiting current. The two slopes intersect at the measured limiting current. The limiting current I_{lim} is related to the limiting current density i_{lim} via Eq. (2). This method is demonstrated in Section 4.1.

3.6. Desalination rate experiments

To validate the mass-transfer (Section 2.3) and electrical (Section 2.2) models, both the bench-scale and commercial-scale systems were operated in constant voltage, batch recirculation mode over

Table 4
Batch desalination test parameters and results for specific energy and desalination rate. Each bench-scale test (A–C) was run twice. Reported feed and product concentrations were converted from measured conductivity using Eq. Falk. Note that the batch duration can be calculated from the diluate volumes and desalination rates provided.

	Bench-scale			Commercial-scale		
	Test A	Test B	Test C	Test D	Test E	Test F
Applied voltage [V]	8.0	10.0	11.0	40.0	35.0	25.0
Stack flow rate [L/h]	40	80	70	1860	1260	1260
Feed concentration [mg/L]	3040	2955	2958	3451	3201	3526
	3216	2987	3063			
Product concentration [mg/L]	182	99	176	480	507	395
	178	136	195			
Concentrate volume[L]	1	1	0.25	204	204	204
Diluate volume [L]	1	1	1	757	757	757
Resultant recovery ratio	0.5	0.5	0.8	0.8	0.8	0.8
Modeled desal specific energy [kWh/m^3]	0.88	1.12	1.26	1.03	0.83	0.71
	0.97	1.11	1.30			
Experiment desal specific energy [kWh/m^3]	0.92 ± 0.03	0.96 ± 0.04	1.13 ± 0.04	1.13 ± 0.02	0.87 ± 0.01	0.73 ± 0.01
	0.82 ± 0.03	1.19 ± 0.05	1.04 ± 0.05			
Modeled desalination rate [L/h]	1.88	2.30	2.58	661	522	338
	1.70	2.44	2.57			
Experiment desalination rate [L/h]	1.88 ± 0.05	3.00 ± 0.08	2.15 ± 0.06	650 ± 10	496 ± 7	375 ± 5
	2.22 ± 0.06	3.00 ± 0.08	2.22 ± 0.06			

the conditions shown in Table 4. Bench-scale stack tests were replicated and both test results are shown. Commercial-scale stack tests were performed once due to the extended setup time required to prepare large batches of NaCl solution.

3.7. Entrance pressure drop experiments

Along with measuring the total pressure drop across the full commercial stack, we also conducted an experiment to isolate the pressure drop contribution associated with the entrance flow into its channels. The results were compared to the pressure drop predicted by the channel models presented in Section 2.7.1, and used to estimate the relative contribution of entrance effects to the total pressure drop.

For this experiment, the entrance sections from several MkIV-2 U-shaped flow-spacers (Fig. 7 (i)) were trimmed to isolate the feed port and initial expansion into the channel (Fig. 7 (ii)). A set of trimmed spacers were sandwiched between two 1 cm thick aluminum end plates, with membranes spaced between them. An adapter, machined from Delrin, was added at the inlet of this assembly to receive flow from a horizontal 5.1 cm ID (2 in.) PVC pipe (Fig. 7 (iii)). Pressure drop was measured using either 5 spacers or 20 spacers, with all membranes and spacers rinsed between tests using Cambridge city tap water.

A Flotec FP5172 pump was used to provide between 0.35 and 1.15 L/min of water flow into the stack, controlled manually using a butterfly valve, with flow rate measured at a frequency of 1 Hz upstream of the experimental assembly using an Omega FP1402 sensor (± 0.2 L/min). The pressure was also monitored at 1 Hz with Omega PX309 pressure gauges (± 2%) at two positions: 60 cm before the stack entrance (Point A), and after the flow has passed through the contraction, at the exit (Point B). The difference between the two pressure measurements was attributed to entrance losses.

3.8. Error calculations

For desalination, limiting current density, and pressure drop experiments on the bench-scale stack (including tests A–C), error is reported as the sensor accuracy. Since the measurements were obtained manually, the error associated with sampling frequency is substantial, and therefore is also presented. For corresponding tests on the commercial-scale stack (including tests D–F), error is reported as the quadrature of the sensor accuracy and the 95% confidence interval over 30–60 measurements taken at 1 Hz. When calculated values are reported (specific energy, production rate, current density, linear velocity, and current efficiency), standard error propagation rules have been applied for both systems.

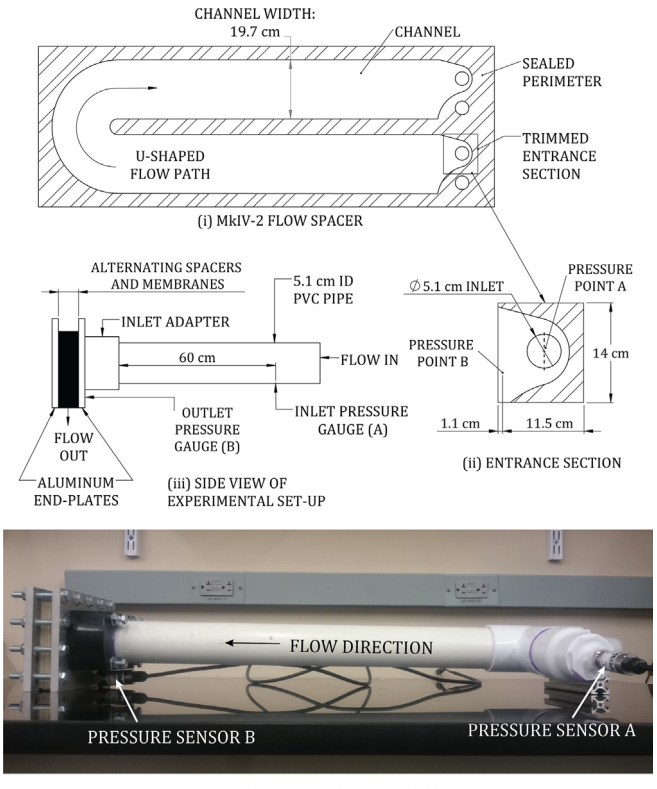

Fig. 7. Entrance sections of several MKIV-2 flow spacers (i) were cut to isolate the inlet and initial expansion into the channel (ii). Pressure drop was measured for varying flow rates through a set of membranes and entry sections, sandwiched between two aluminum plates (iii), in the experimental apparatus photographed above (iv).

4. Results and model validation

In this section we compare model predictions and experimental

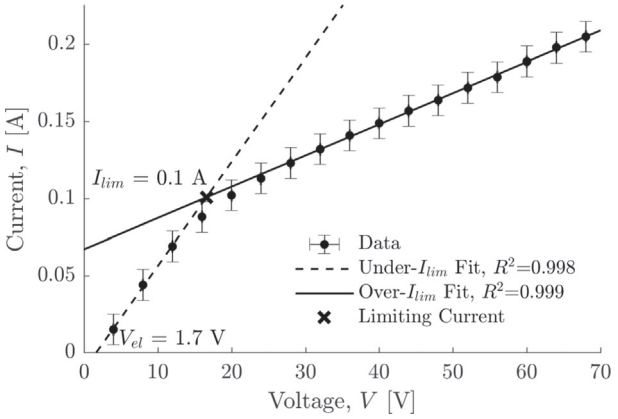

Fig. 8. Example limiting current test. Measured current I plotted against applied voltage V for a 250 mg/L NaCl solution at a flow rate of 30 L/h in the bench-scale stack. The limiting current I_{lim} is estimated at the intersection of the two distinct linear regions: under-limiting current (dashed line) and over-limiting current (solid line).

results for limiting current density, desalination rate, and pressure drop on the bench-scale and commercial-scale stacks.

4.1. Limiting current density validation

Fig. 8 demonstrates the method of determining limiting current for a 250 mg/L NaCl feed solution at a flow rate of 30 L/h in the bench-scale ED stack. The intercept of the under-limiting curve with the horizontal (voltage) axis also provides an experimentally determined electrode potential E_{el} of 1.7 V, which is close to the expected standard cell potential of 1.4 V (described in Section 2.2).

Results from the limiting current density tests for the bench-scale and commercial-scale stacks are shown in Fig. 9. As expected, i_{lim} increases linearly with conductivity (which is proportional to NaCl concentration over the range evaluated) and increases with flow rate (Fig. 9). Measurements of i_{lim} matched closely with theoretical predictions for both the bench-scale and commercial-scale stacks, thereby validating the limiting current density model presented in Section 2.5 for both stack size scales.

For a given conductivity and flow rate, the measured i_{lim} is significantly lower for the commercial-scale stack (Fig. 9b) than the bench-scale stack (Fig. 9a). In an ED stack, the actual limiting current density is approached towards the very end of the flow path where diluate concentration is the lowest, while the measured current density is the average over the entire flow path. For the bench-scale stack, this difference between the measured (average) current density and actual limiting current density is small because of the short spacer channel length; for the commercial stack, the flow path is long enough for this difference to become measurable, thereby reducing the measured i_{lim} relative to the bench-scale stack.

4.2. Desalination rate validation

Fig. 10 compares the predicted and measured conductivity trajectories across the array of test conditions listed in Table 4. Overall, there is good agreement between experimental results and model predictions for both the bench-scale and commercial-scale stack. The desalination rate was 1–23% higher than predicted for tests A and B, and 16–20% lower than predicted for test C using the bench-scale stack. The desalination rate was 2–4% lower than predicted for test D and E, and 11% higher than predicted for test F using the commercial-scale stack. The desalination rate could be higher than expected because (1) the measured area porosity is lower than the actual area available for ion transport, as explored in Section 5.1; or (2) the modeled membrane resistance was too high, resulting in under-prediction of the current, as explored in Section 5.5. While prediction, particularly for the bench-scale test could be improved with further membrane characterization, in general, the model agrees well with the experiments.

4.3. Pressure drop validation

Fig. 11 compares the experimentally measured pressure drop for both stacks to the four models presented in Section 2.7. These comparisons use the measured void fraction $\epsilon = 0.83$ for the commercial-scale spacer and $\epsilon = 0.60$ for the bench-scale spacer, except for the correlation based on Ponzio's data, which is valid only for a single void fraction of $\epsilon = 0.80$.

For the overlapped spacer in the commercial stack, all models under-predict the measured pressure drop. While Ponzio's model provides the best alignment in terms of trend and magnitude, it still underpredicts the experimental result by 37% at the manufacturer-recommended linear flow velocity of 7 cm/s.

The bench-scale stack contained a woven spacer. While Gurreri et al.'s woven spacer model predicts within an average of 9.4% of the measured pressure drop, $\epsilon = 0.60$ falls outside the domain investigated in their work ($0.76 < \epsilon < 0.88$). As described in Section 2.7.4, Eqs. (36) and (37) are power laws fitted to Gurreri et al.'s data and extrapolation may result in invalid pressure drop predictions. For example, if a linear fit were implemented, then the resulting model would predict a pressure drop that is 36% of the model values plotted in Fig. 11.

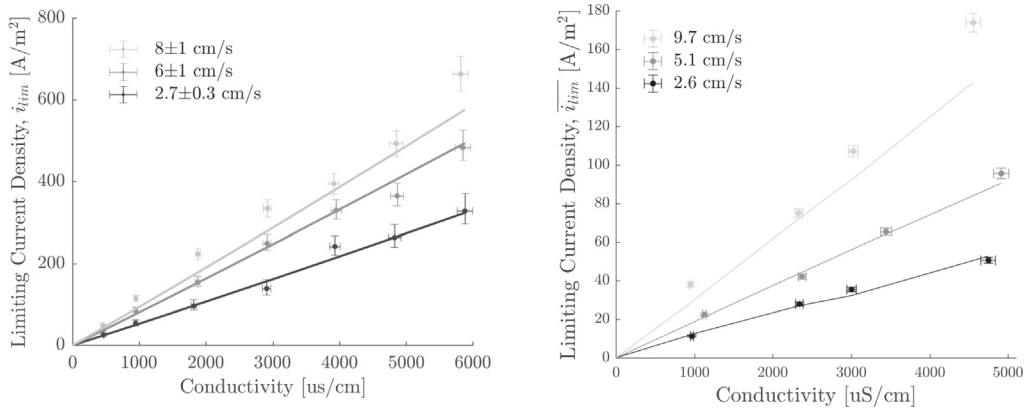

(a) Bench-Scale Stack (b) Commercial-Scale Stack

Fig. 9. The limiting current density i_{lim} plotted against the input solution conductivity for varying flow rates, measured using the bench-scale test stack (a) and the commercial-scale test stack (b). Solid lines are model predictions; points are experimental data.

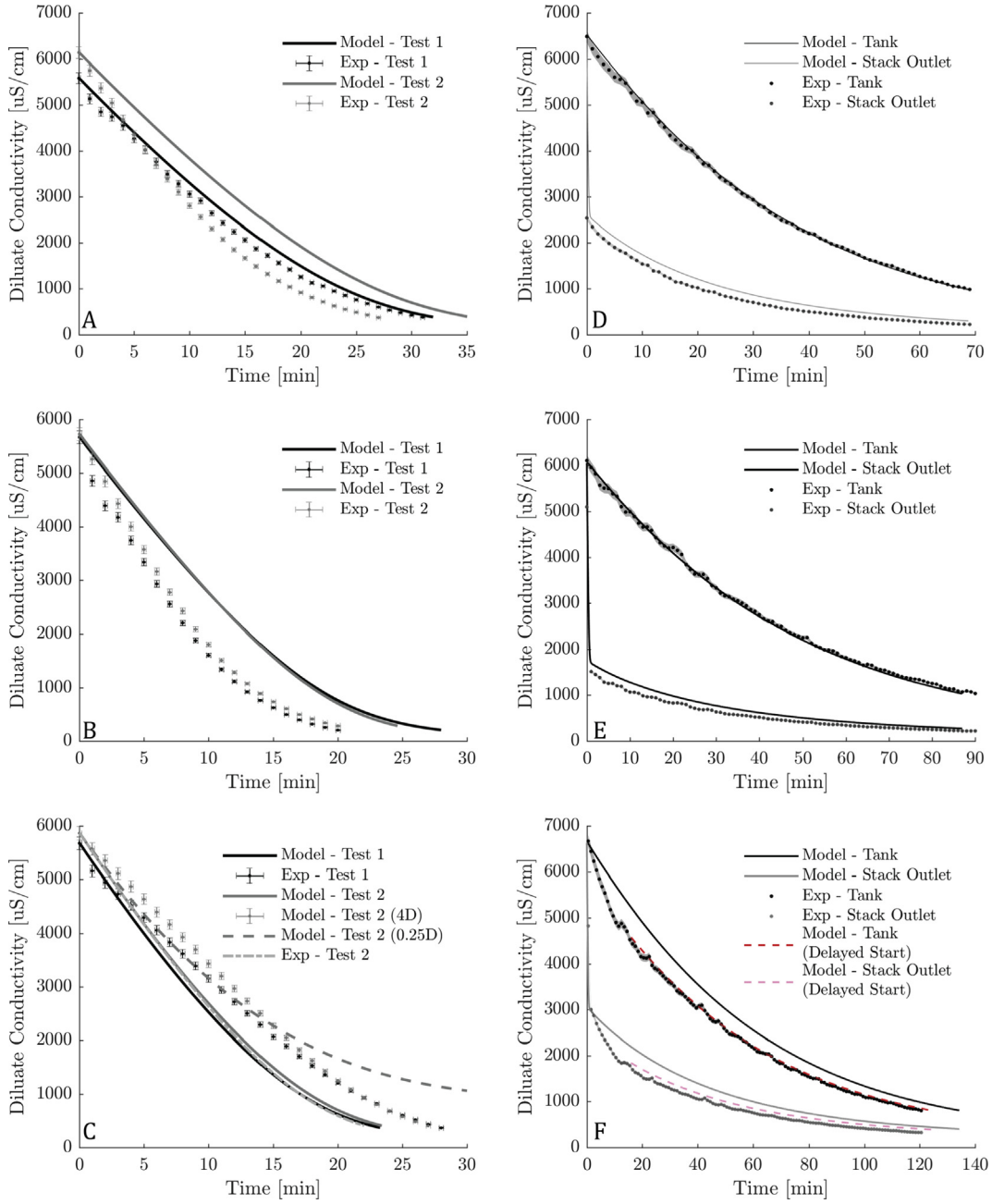

Fig. 10. Measured and modeled diluate tank conductivity is plotted against time for bench-scale tests (A–C). For the commercial-scale stack (D–F), diluate conductivity within the tank and at the stack outlet are both plotted against time. When test C is modeled with a higher membrane diffusion constant of 4*D*, diffusion balances ion migration, and the desired concentration is never achieved ($D^{AEM} = D^{CEM} = D$). The results for test F are shown with both a standard model start (both tanks at the feed water salinity) and with a delayed model start time shifted by 15 min to show how early errors in the model and/or sensing are propagated through the trial.

We also investigated if entrance effects into the channel could account for the observed difference between the channel model predictions and measured pressure drops using the setup described in Section 3.7. The results of this test for 5 and 20 spacers is shown in Fig. 12. The test confirms that (1) the entrance losses act in parallel with one another, because the same volumetric flow rate per cell Q^{cell} produces the same pressure drop, and (2) the entrance effects account for < 1% of the total pressure drop for the commercial-scale stack. For example, at a typical channel velocity of 7 cm/s, the entrance effect contributes only 0.9 kPa to the total of ≈100 kPa seen for the full stack (Fig. 11).

Although models were identified that could predict channel pressure drop relatively accurately for the two stacks used in this study (Gurreri et al. for the bench-scale stack, and Ponzio et al. for the commercial stack), a single model that could be applied for a variety of stack sizes and conditions was not identified. Furthermore, Gurreri et al.'s model is highly sensitive to how it is extrapolated for void fractions outside the authors' original work. We caution other researchers against choosing a specific model to predict channel pressure drop, and thus pumping power, for a given stack design; it may be necessary to conduct experiments to fully characterize a spacer's pressure drop behavior. We conclude that the existing pressure drop models under-predict real channel losses, considering that entrance effects to the channels and other losses associated with inlet and outlet piping to the stack are negligible (Appendix A).

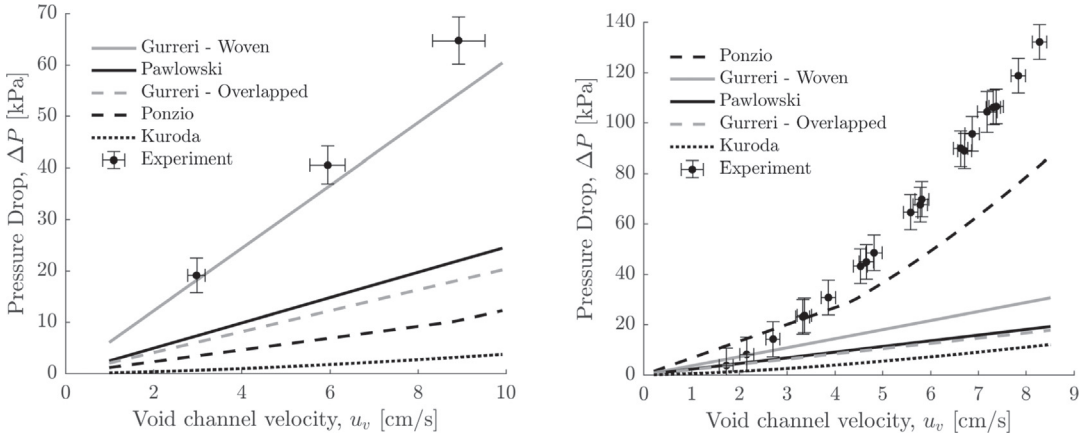

Fig. 11. Modeled and experimental pressure drop for the bench-scale stack (ϵ = 0.60, left) and for the commercial-scale stack (ϵ = 0.83, right). All four models under-predict the experimental values. Gurreri et al.'s woven model provides good alignment for the bench-scale test but under-predicts the pressure loss on the commercial-scale stack. Additionally, ϵ = 0.60 is outside of the range over which the model was derived (0.76 < ϵ < 0.88). Ponzio et al.'s model provided the closest alignment with the commercial-scale data, but still under-predicted measured values by 37% at the manufacturer recommended flow velocity of 7 cm/s.

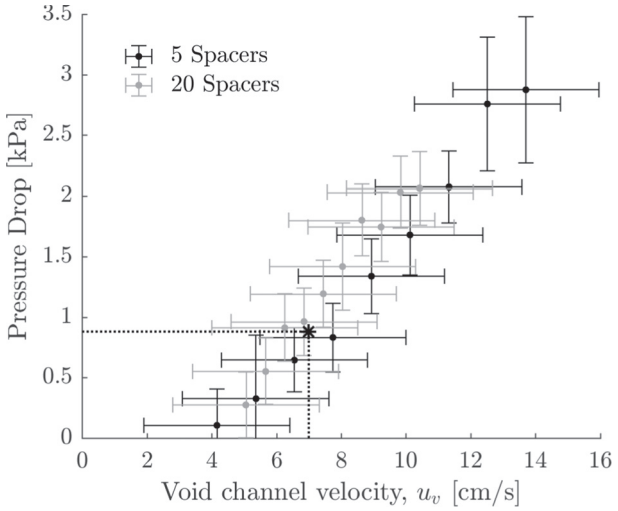

Fig. 12. Experimental results showing the pressure drop over the inlet only for the spacer used in the commercial-scale tests. The pressure drop for 5 spacers and 20 spacers is approximately the same when the channel velocity is held constant. Dotted lines mark a typical channel velocity for this spacer of 7 cm/s; at this velocity the entrance effect contributes only 0.9 kPa to the total of ≈100 kPa seen for the full stack.

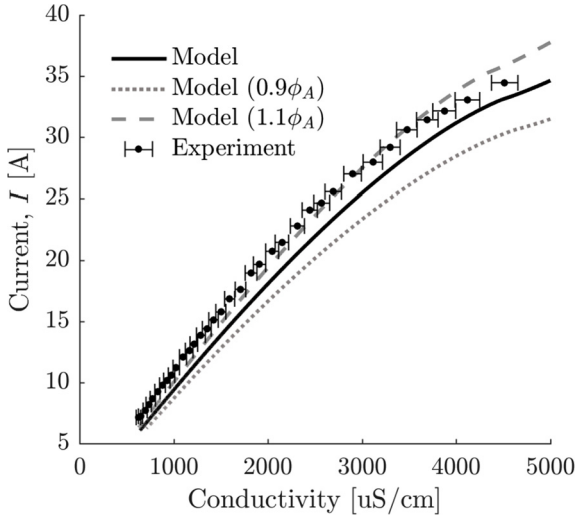

Fig. 13. Model prediction and measured total current as a function of the average conductivity between the stack inlet and outlet for Test D. The gray dashed and dotted lines represent a ± 10% sensitivity band on the prescribed area porosity (ϕ_A = 0.70). Error in conductivity measurements are shown as horizontal error bars, while error in current measurements is smaller than the plotted dot size.

5. Discussion on model sensitivity

In this section we examine the sensitivity of the model predictions to the simplifying approximations presented in Section 2. Comparison is performed using the commercial-scale stack because it is more relevant for industrial electrodialysis processes. Model sensitivity was analyzed for Test D because the operating void channel linear velocity (6.8 cm/s) most closely matches manufacturer recommendations [39].

5.1. Sensitivity to area porosity

Fig. 13 demonstrates relatively good agreement between model predictions of total current to measured values for Test D, with an under-prediction at all conductivities. This small systematic error is achieved without the use of any empirically derived parameters or prior system characterization requirements.

One possible explanation for the under-prediction of current in Fig. 13 is the uncertainty in the fractional membrane area available for ion transport, since it could be higher or lower than the open area of the spacer, resulting in a different effective value of ϕ_A. Here we investigate if the measured open-area porosity is a good measure of the actual fractional membrane area available for ion transport.

To test whether the measured porosity is a reasonable approximation, we examined the effect on current predictions if the actual fractional area were ± 10% from the measured open-area porosity of the spacer of ϕ_A = 0.7. The predicted current changes by very little (Fig. 13), thereby indicating that the accuracy is not significantly affected by this approximation. This result is significant because it implies that the open-area porosity of the flow-spacer can be used to estimate the fractional membrane area that will participate in desalination. Furthermore, the area porosity was measured in this study, but it is usually provided by mesh suppliers. Therefore, a designer can avoid additional measurements and use the vendor-specified values to perform initial sizing and current calculations.

5.2. Sensitivity to void fraction

While both the mass transfer rate and pressure drop depend on the void fraction, ϵ, the effect on the desalination energetics is not as significant as for pumping. The sensitivity of the pressure drop to void fraction is high, as shown via the friction factor correlations for all models (Fig. 5). As an example, consider the effect of the void fraction measurement error (± 0.04, Table 2) on the predicted pressure drop for the bench-scale stack, operating at 7 cm/s, and using the best-fit pressure drop model from Fig. 11a (Gurreri-Woven). If $\epsilon = 0.56$, the modeled pressure drop would increase by 63%, from 42.6 to 69.3 kPa. If $\epsilon = 0.64$, the modeled pressure drop would decrease by 37% to 27.0 kPa. As small errors in void fraction can lead to substantial differences in predicted pressure drop, especially for thin spacers, it is recommended that researchers aim to reduce void fraction measurement error as much as possible and that designers consider realistic manufacturing tolerances. Additionally, the thickness of the sealing edge of the spacer relative to the thickness of the mesh itself, and the applied torque at the tie rods which act to compress the membranes and spacer together, could both affect the actual void fraction.

The void fraction also affects the limiting current density and the mass transfer rate because of the dependence of the mass transfer coefficient k on the spacer-filled channel velocity u_{ch} (Section 2.6). The sensitivity in this case is lower than for pressure drop, however, since k primarily affects the concentration at the surface of the membrane, which in turn affects the rate of back diffusion, the boundary layer resistances, and the membrane potential, which are not the dominant impedances in brackish water ED (Sections 2.2.1, 5.4, and 5.5).

5.3. Sensitivity to model discretization

The effect of discretizing the flow-path from 1 to 10 segments on current predictions is examined, and compared to measured values for Test D (Fig. 14). Use of a single segment ($Y = 1$) under-predicts the initial current by 15.8%, while use of 10 segments ($Y = 10$) under-predicts by only 2.7%. Increasing from 1 segment to 2 segments results in approximately the same improvement, with 1.8× higher computational cost, as increasing from 2 segments to 10 segments, with a compounded 4× increase in computational time. Therefore, as Y increases, it is important to consider the trade-off between improved accuracy and longer computation time (Table 5).

Increasing the number of discretizations is important when modeling stacks with long flow paths, such as the commercial-scale stack. Here, the assumption that the entire channel is well mixed becomes less accurate. With shorter flow paths, such as the bench-scale stack, discretization is less important. For example, increasing from 1 to 20 segments in Test A produced a difference of only 5% in predicted desalination rate.

Table 5
Computation time for Y = 2, 5 and 10 segments, relative to computation time if a single segment (Y = 1) is used for Test D for the commercial-scale stack.

Number of segments, Y	Relative computation time
1	1.0
2	1.8
5	4.1
10	7.7

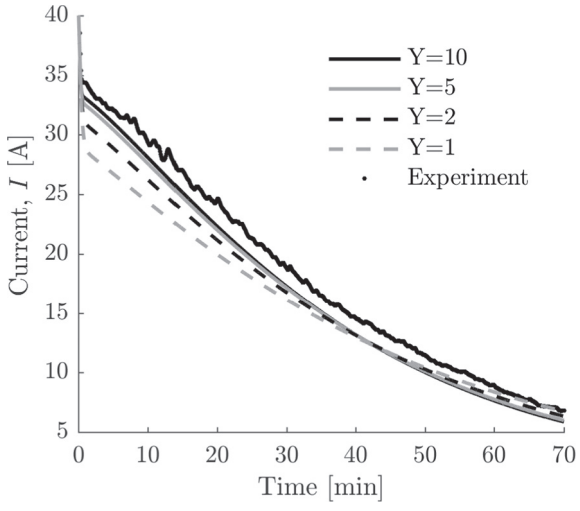

Fig. 14. Model predictions and measured values of total current for Test D. The effect of segmenting the stack into Y = 1, 2, 5, and 10 segments is shown. With fewer segments, the model under-predicts the total current. Error on the current measurement is smaller than the dots shown.

5.4. Sensitivity to membrane diffusion

Current efficiency is the ratio of the net rate of ion transfer to the expected rate, given a current.

$$\eta = \frac{(C_{d,0} - C_{d,Y})Q_d^{\text{cell}}F}{I_{\text{total}}} \tag{44}$$

Current efficiency may be less than 1.0 because of several factors. Back diffusion of ions from the concentrate to the diluate may be non-negligible (Eqs. (14) and (15)), particularly when $C_c >> C_d$ such as at the end of a batch or near the stack outlet. Current leakage can also occur through a path parallel to the active channel area, if the membrane stack is not electrically insulated adequately.

A comparison of modeled and experimental current efficiency (Fig. 15) shows good agreement. At the start of the test, when back diffusion is negligible, current efficiency is approximately 1.0, making it reasonable to assume that current leakage is also negligible for the stack tested. Strong alignment towards the end of the batch also suggests that values assumed for the membrane diffusion coefficients ($D^{AEM} = D^{CEM} = D$) are reasonable.

Sensitivity to the membrane diffusion coefficient on current efficiency was modeled by increasing and decreasing the membrane diffusion coefficient by a factor of four: 4D and 0.25D (Fig. 15). In both cases, the predicted current efficiency deviated significantly from the measured values, particularly at the end of the batch where the difference between the diluate and concentrate concentrations is the

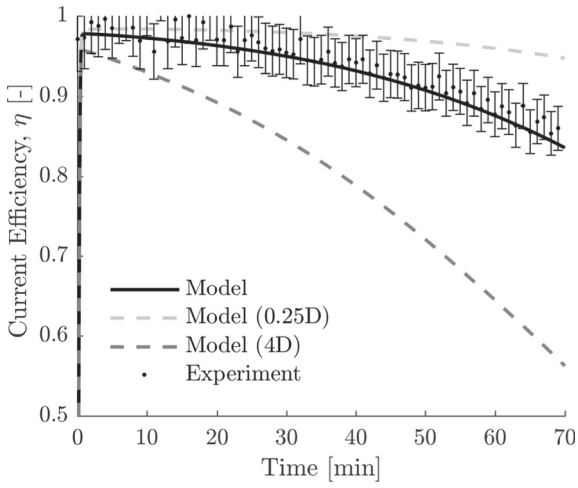

Fig. 15. Model and experimental results for current efficiency vs. time for Test D. The results are shown with the model sensitivity to the membrane diffusion coefficient, $D^{AEM} = D^{CEM} = D$.

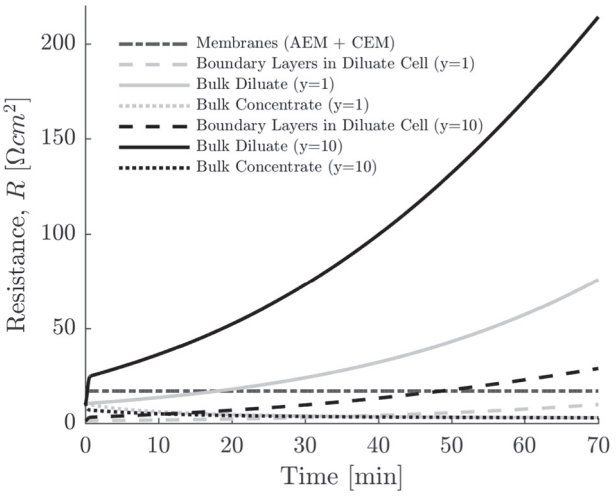

Fig. 16. The modeled individual resistances for a single cell pair in first segment ($y = 1$) and final segment ($y = Y = 10$) during Test D.

largest. For example, a membrane coefficient of 4*D* under-predicts the current efficiency (and thus the quantity of salt removed) by 34% at this point. Note that 4*D* represents an extreme case where, for example in Test C (Fig. 10), the model predicts that the desired concentration would never be achieved.

5.5. Sensitivity to membrane and boundary layer resistances

The total electrical resistance of the stack is made up of membrane, bulk, and boundary layer resistances as described in Eq. (4). The modeled contribution of each resistance in the first and last segment of the stack during Test D is shown in Fig. 16. The contribution of the resistance from the boundary layer in the concentrate channel was negligible and therefore omitted from the figure. While both the membranes and the bulk diluate resistance are important in the first segment, the bulk diluate resistance always provides the largest contribution in the last segment, accounting for more than 50% of the resistance after 10 min, and 89% at the conclusion of the batch. This relative importance would continue to increase if the batch were desalinated to even lower salinity.

As discussed in Section 2.2.1, the membrane resistance has been shown to change with the concentration on either side of the membrane. Specifically, Długołęcki et al. found that the resistance of the membrane varied inversely with the solution conductivity [27]. The resistance of the membranes used in the commercial-scale tests was characterized by the manufacturer using a 0.01 M solution. In Fig. 16 a diluate concentration of 0.01 M is achieved at approximately 50 min, at which point the membrane resistance is a small percentage of the total resistance. Using the relationship observed by Długołęcki et al., a static resistance over-predicts the actual resistance at all times prior to this point and helps explain the discrepancy between experimental and modeled conductivity observed in all tests (Fig. 10). If the modeled static resistance is too high at the beginning of the trial, it results in lower applied current, and fewer ions are removed, resulting in lower initial desalination rates than measured. Because the experiment is operated in batch mode, that error propagates throughout the entire test.

5.6. Sensitivity to water transport

Water transport across the membranes due to osmosis and electro-osmosis was not included in the model validation results presented in this study. Experiments on the commercial-scale stack did reveal a volume increase in the brine tank and corresponding volume decrease in the diluate tank during all tests. The model was rerun including water transport for Test D per Eqs. (20) and 21. The predicted increase in brine volume was 14 L while the experimentally observed increase was 19 ± 3 L. The difference in specific energy consumption between the model results without water transport (1.03 kWh/m^3) and with water transport (1.04 kWh/m^3) is approximately 0.01% and thus negligible, consistent with the original assumption. It should be noted, however, that at high recoveries, water transport could constitute a non-negligible effect on the total brine volume (which needs to be disposed of properly and thus affects system cost). For example, the 19 L of additional brine due to water transport in Test D constitutes an increase of 9% from the original volume and reduces the overall water recovery by 2%.

5.7. Validity for multi-ion solutions

The model presented in this work considers a single 1-1 electrolyte that comprised only of NaCl, following the practice used in previously published ED models. This assumption is the basis for selecting the Onsager/Falkenhagen equation to translate conductivity to molar concentration and for selecting all diffusion coefficients and transport numbers. Real brackish groundwater contains multiple ions and exhibits a more complicated relationship between conductivity and molarity than for NaCl alone [26]. To explore the implications of this simplification, we conducted a test of the GE commercial-scale stack using real groundwater from a well in Chelluru, India.

Feed water composition was measured by a private laboratory in India with National Accreditation Board Laboratory (NABL) certification (Care Labs, Hyderabad, India), and is given in Table 6. Concentrations of Na^+, Mg^{2+}, Ca^{2+}, Cl^-, Alkalinity, TDS, and conductivity were measured following APHA procedures 3500-Na-B, 3500-Mg-B, 3500-Ca-B, 4500-Cl-B, 2320-B, 2540-C, and 2510-B, respectively [40], and SO_4^{2-} following IS:3025(Pt-24) [41]. Errors were estimated following [40],[42], and [43]. The laboratory measured total TDS and conductivity of the feed water was used to calculate a conversion factor of 0.6, used in all subsequent conversions.

A commercial ED stack of the same configuration as the commercial-scale stack used in Tests D–F was tested in Chelluru, with all parameters held at the same values presented in Tables 2 and 3. A locally sourced power supply was used to apply 40 ± 1 V at the electrodes. Current was measured at 1 Hz using a CR Magnetics CR5210-30 DC current transducer (1% accuracy). Temperature was between 27 and 28° C. For this test, the stack produced 500 L of 300 mg/L TDS water, at recovery of 40%. The average flow rate through the stack was 27.6 L/min.

Figs. 17 and 18 show the model and experimental results from a single trial, while Fig. 19 shows the averaged results for 11 trials completed over 2 days.

The model specific energy and production rate results (0.31 kWh/m^3, 0.85 m^3/h) matched the experimental results (0.39 kWh/m^3, 0.71 m^3/h) well for the multi-ion feed. This is primarily because the

Table 6
Concentration of major constituents in the raw water used for the test in Figs. 17 and 18. The final column shows the molar mass to charge ratio (M/z) for each constituent, where the ratio for CO_3^{2-} is shown in the alkalinity row.

Parameter	Value	M/z
Na^+ [mg/L]	142 ± 25	23
Mg^{2+} [mg/L]	66.8 ± 6.3	12
Ca^{2+} [mg/L]	230 ± 22	20
Cl^- [mg/L]	382 ± 37	35
SO_4^{2-} [mg/L]	72.4 ± 6.6	48
Alkalinity (HCO_3^-) as $CaCO_3$ [mg/L]	648 ± 56	30
TDS [mg/L]	1490 ± 103	
Conductivity [uS/cm]	2480 ± 55	

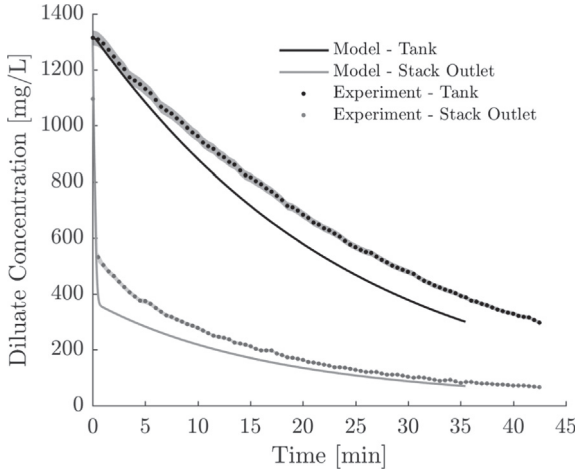

Fig. 17. Modeled and experimental diluate tank concentration and stack outlet concentration vs. time for the test using real groundwater (Table 6). Model is given as concentration in mg/L of NaCl. Experiment as concentration in mg/L of the multi-ion solution, using a conversion 0.6 × Conductivity (uS/cm) = Concentration (mg/L). Experimental error is shown as a gray band around the data points.

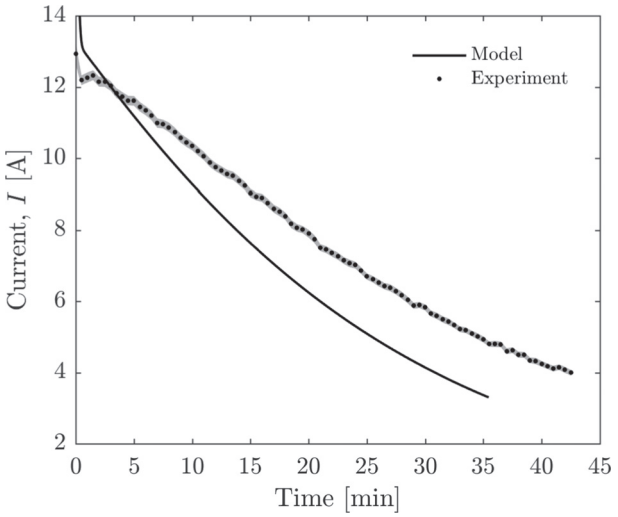

Fig. 18. Modeled and experimental total applied current vs. time for the test using real groundwater (Table 6). Experimental error is shown as a gray band around the data points.

molar mass to charge ratio for the divalent positive and negative ions is on the same order as for Na^+ and Cl^-, respectively (Table 6). Because of this, the movement of ions due to migration is also on the same order (Eqs. (14) and (15)).

Fig. 19 shows that at any given diluate tank concentration, the predicted conductivity is higher than the measured conductivity. This results in a predicted resistance that is lower than the actual resistance, and predicted current that is higher than the measured current, explaining the higher production rate predicted by the model (Fig. 17). Should a more accurate prediction of production rate and specific energy be required, conductivity and membrane transfer number models that account for the presence of multiple ions should be used.

6. Conclusions

This work presents a robust model of brackish water electrodialysis (ED) that predicts desalination rates, current, limiting current density, and energy consumption. The model was experimentally validated at

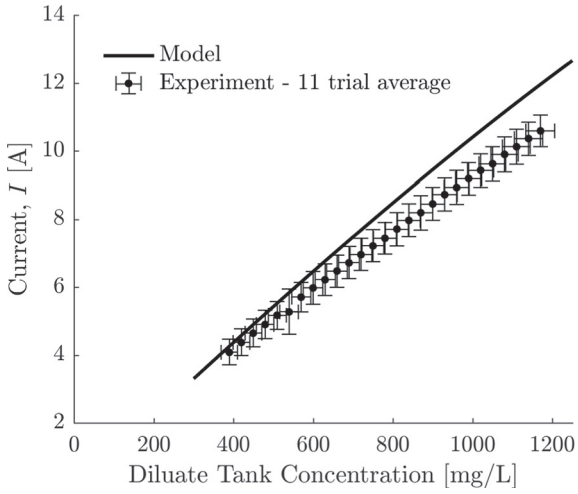

Fig. 19. Modeled and experimental total applied current vs. concentration, averaged over 11 trials completed over 2 days (Table 6).

two diverse stack size scales (0.18 vs. 37.1 m^2 total membrane area), spacer thicknesses (0.35 vs. 0.71 mm), spacer types (woven vs. overlapped), as well as in two diverse feed waters (NaCl vs. real brackish groundwater). The measured desalination rate was within 5–25% and 2–11%, and the measured energy consumption was within 1–23% and 1–9%, of predicted values for the lab-scale and commercial-scale stacks, respectively. This agreement indicates that the mass transport behavior of both stacks was captured with reasonable accuracy. To the authors' knowledge, the theory presented herein is the first robust model of ED systems that does not require any experimental parameter estimation or system characterization.

An objective of this work was to create a full energy consumption model that accounts for both electrochemical and hydraulic contributions. Although power consumption from the ED process was accurately characterized, we were not able to present a single model that reliably predicted pressure drop in the flow channels for both stack sizes and spacer designs. Of the four models for pressure drop that were evaluated, Gurreri et al.'s was the most accurate for the lab-scale stack when extrapolated using a power law relationship (predicting within 9.4%), and Ponzio's was the most accurate for the commercial-scale stack (predicting within 37%). These models may be used to approximate required pumping power for the specific stack architectures tested in this study, but they may not be accurate for alternate stack designs and spacer configurations. Pressure drop and pumping power characterization for ED stacks should be an ongoing area of research. At present, we encourage researchers and ED stack designers to conduct experiments to measure channel spacer pressure drop to form an accurate prediction of required pumping power.

The accuracy of the presented ED model was found to be insensitive to several practical simplifications and assumptions capable of reducing computation time and making the model more amenable to design optimization. These included neglecting water transport, treating the membranes as perfectly ion-selective with static electrical resistances, neglecting the resistance contributions from the concentration boundary layers within the channels, and using the open-area porosity of the spacers to estimate the fractional area available for ion-transport. Experimental data collected from an active pilot ED water treatment plant in Chelluru, India demonstrated the robustness of modeling actual brackish groundwater with multiple charged ions as a pure NaCl solution with an equivalent concentration; predictions of desalination rate and specific energy consumption for real groundwater were found to be accurate within 20 and 22%, respectively.

The theory presented in this work constitutes a powerful tool for electrodialysis researchers and system designers. Its novelty is in

providing a fully parametric description of system behavior, enabling desalination rate and power consumption to be quantitatively predicted before an ED system is built. The theory is agnostic to specific size scales and designs, facilitating the exploration of new ED stack architectures and their optimization.

Notation

Roman symbols

a	Onsager/Falkenhagen constant (-)
B	Onsager/Falkenhagen constant (-)
B_1	Onsager/Falkenhagen constant (-)
B_2	Onsager/Falkenhagen constant (-)
C	molar concentration (mol/m^3)
C^b	bulk concentration (mol/m^3)
C_d	diluate concentration (mol/m^3)
C_c	concentrate concentration (mol/m^3)
C^{AEM}	concentration at surface of AEM (mol/m^3)
C^{CEM}	concentration at surface of CEM (mol/m^3)
d_f	filament diameter (m)
d_h	hydraulic diameter (m)
D^{AEM}	diffusion coefficient of NaCl in AEM (m^2/s)
D^{CEM}	diffusion coefficient of NaCl in CEM (m^2/s)
D_{aq}	diffusion coefficient of aqueous solution (m^2/s)
E_{total}	total applied voltage (V)
E_{el}	electrode potential (V)
E_{mem}	membrane potential (V)
E^{AEM}	membrane potential, across AEM (V)
E^{CEM}	membrane potential, across CEM (V)
f	Darcy friction factor (-)
F	Faraday constant (C/mol)
g	gap between mesh spacer and membrane (m)
h	channel gap (m)
h_{sp}	channel thickness (m)
i_y	current density in segment y (A/m^2)
i_{lim}	limiting current density (A/m^2)
I_{total}	total instantaneous current (A)
k	mass transfer coefficient (m/s)
l_f	filament pitch (m)
l^{AEM}	AEM membrane thickness (m)
l^{CEM}	CEM membrane thickness (m)
L_w	cell pair membrane water permeability (mol/bar-m^2-s)
Lv	flow path length (m)
M	molar mass (kg/mol)
N	number of cell pairs (-)
P	pressure (Pa)
Q	flow rate (m^3/s)
R	gas constant (J/mol-K)
R_d^b	area resistance, bulk diluate (Ωm^2)
R_c^b	area resistance, bulk concentrate (Ωm^2)
R^{AEM}	area resistance, AEM (Ωm^2)
R^{CEM}	area resistance, CEM (Ωm^2)
R^{BL}	area resistance, boundary layers (Ωm^2)
t	time (s)
t^{AEM}	transport number, anions in AEM (-)
t^{CEM}	transport number, cations in CEM (-)
t_+	transport number, cations in solution (-)
t_-	transport number, anions in solution (-)
t_w	cell pair water transport number (-)
T	temperature (K)
u_{ch}	spacer-filler channel velocity (m/s)
u_v	void channel velocity (m/s)
V^{cell}	volume in single stack cell/channel
V^{tank}	volume of batch recirculation tank
W	flow path width (m)
y	segment (-)
Y	total number of segments (-)
z	ion charge number (-)

Greek symbols

γ	activity coefficient (-)
Γ_{total}	total specific energy (J/m^3)
Γ_{desal}	specific energy of desalination (J/m^3)
Γ_{pump}	specific energy of pumping (J/m^3)
δ	boundary layer thickness (m)
ϵ	void fraction (-)
η	current efficiency (-)
η_{pump}	pump efficiency (-)
λ_C	equivalent conductance at concentration C (Scm^2/mol)
λ_0	equivalent conductance at infinite dilution (Scm^2/mol)
μ	viscosity of aqueous solution (Pa-s)
π	osmotic pressure (bar)
ρ_{aq}	density of aqueous solution (kg/m^3)
ρ	solution resistivity (m)
ϕ_A	area porosity (-)
ϕ	current leakage factor (-)

Acknowledgments

This work was sponsored by Tata Projects, Ltd., UNICEF, USAID, Eureka Forbes Ltd., the Tata Center for Technology and Design at MIT, and the National Science Foundation Graduate Research Fellowship under grant no. 1122374.

Appendix A. Pipe loss calculation

Table A.7
Major and minor losses in the pipe components between the pressure gauges and the stack spacers.

Major losses	Length	Friction factor, f	Pressure drop [kPa]
5.08 cm diameter pipe	2 m	0.031	0.04
Minor losses	**Quantity**	**Loss coefficient, k_L**	**Pressure drop [kPa]**
Expansion from 2.54 cm diameter pipe to 5.08 cm diameter pipe	1	0.55	0.32
45° bend in 5.08 cm diameter pipe	2	0.4	0.03
90° bend in 5.08 cm diameter pipe	2	1.5	0.11
Contraction from 5.08 cm diameter pipe to 2.54 cm diameter pipe	1	0.4	0.24

In Section 4.3 it is stated that the pressure drop over the components between the pressure gauges and the entrance/exit to the stack contributes negligibly to the total loss. These effects were approximated using the Darcy-Weisbach equation for fully developed, steady, incompressible flow in the straight pipe sections (major losses),

$$\Delta P = f\frac{l}{D_{pipe}}\rho\frac{V^2}{2}, \tag{A.1}$$

and standard loss coefficients for the minor losses,

$$\Delta P = \rho k_L \frac{V^2}{2} \tag{A.2}$$

where f is the friction factor, obtained from a Moody chart, l is the pipe length, D_{pipe} is the diameter of the pipe, ρ is the fluid density, V is the relevant fluid velocity, and k_L is the minor loss coefficient associated with the various components.

The pressure drop was calculated over all components in the commercial-scale stack at a volumetric flow rate of 33 L/min, set to match a stack void channel velocity of 7 cm/s. The resulting major and minor losses are shown in Table A.7. The total of 0.74 kPa represents less than 1% of the total stack pressure drop.

References

[1] Desaldata, Analysis, 2017.
[2] N.C. Wright, A.G. Winter, Justification for community-scale photovoltaic-powered electrodialysis desalination systems for inland rural villages in India, Desalination 352 (2014) 82–91.
[3] R.K. McGovern, S.M. Zubair, J.H. Lienhard V, The cost effectiveness of electrodialysis for diverse salinity applications, Desalination 348 (2014) 57–65.
[4] K.M. Chehayeb, D.M. Farhat, K.G. Nayar, J.H. Lienhard V, Optimal design and operation of electrodialysis for brackish-water desalination and for high-salinity brine concentration, Desalination 420 (2017) 167–182.
[5] K.G. Nayar, P. Sundararaman, J.D. Schacherl, C.L. O'Connor, M.L. Heath, M.O. Gabriel, S.R. Shah, N.C. Wright, A.G. Winter V., , Feasibility study of an electrodialysis system for in-home water desalination in urban India, Dev. Eng. 2 (2016) 38–46.
[6] REvivED Consortium, Low energy solutions for drinking water production by a REvival of ElectroDialysis systems 2016.
[7] H. Strathmann, Electrodialysis, a mature technology with a multitude of new applications, Desalination 264 (3) (2010) 268–288.
[8] A.E. Midaoui, F. Elhannouni, M. Taky, L. Chay, M. Sahli, L. Echihabi, M. Hafsi, Optimization of nitrate removal operation from ground water by electrodialysis, Sep. Purif. Technol. 29 (3) (2002) 235–244.
[9] C. Xue, Q. Chen, Y.-Y. Liu, Y.-L. Yang, D. Xu, L. Xue, W.-M. Zhang, Acid blue 9 desalting using electrodialysis, J. Membr. Sci. 493 (2015) 28–36.
[10] J.-H. Chang, C.-P. Huang, S.-F. Cheng, S.-Y. Shen, Transport characteristics and removal efficiency of copper ions in the electrodialysis process under electroconvection operation, Process Saf. Environ. Prot. 112 (2017) 235–242 challenges in Environmental Science and Engineering CESE 2016.
[11] M. Sadrzadeh, A. Kaviani, T. Mohammadi, Mathematical modeling of desalination by electrodialysis, Tenth International Water Technology Conference, Alexandria, Egypt, 2006, pp. 221–233.
[12] J.M. Ortiz, J.A. Sotoca, E. Expósito, F. Gallud, V. García-García, V. Montiel, A. Aldaz, Brackish water desalination by electrodialysis: batch recirculation operation modeling, J. Membr. Sci. 252 (1-2) (2005) 65–75.
[13] M. Fidaleo, M. Moresi, Optimal strategy to model the electrodialytic recovery of a strong electrolyte, J. Membr. Sci. 260 (1-2) (2005) 90–111.
[14] Z. Zourmand, F. Faridirad, N. Kasiri, T. Mohammadi, Mass transfer modeling of desalination through an electrodialysis cell, Desalination 359 (2015) 41–51.
[15] S. Pawlowski, P. Sistat, J.G. Crespo, S. Velizarov, Mass transfer in reverse electrodialysis: flow entrance effects and diffusion boundary layer thickness, J. Membr. Sci. 471 (2014) 72–83.
[16] H.-J. Lee, F. Sarfert, H. Strathmann, S.-H. Moon, Designing of an electrodialysis desalination plant, Desalination 142 (2002) 267–286.
[17] M.S. Isaacson, A.A. Sonin, Sherwood Number and friction factor correlations for electrodialysis systems, with application to process optimization, Ind. Eng. Chem. Process Des. Dev. 15 (1976) 313–321.
[18] S. Thampy, G.R. Desale, V.K. Shahi, B.S. Makwana, P.K. Ghosh, Development of hybrid electrodialysis-reverse osmosis domestic desalination unit for high recovery of product water, Desalination 282 (1418) (2011) 104–108.
[19] E. Brauns, W. De Wilde, B. Van den Bosch, P. Lens, L. Pinoy, M. Empsten, On the experimental verification of an electrodialysis simulation model for optimal stack configuration design through solver software, Desalination 249 (2009) 1030–1038.
[20] S. Pawlowski, J.G. Crespo, S. Velizarov, Pressure drop in reverse electrodialysis: experimental and modeling studies for stacks with variable number of cell pairs, J. Membr. Sci. 462 (2014) 96–111.
[21] M. Johannink, K. Masilamani, A. Mhamdi, S. Roller, W. Marquardt, Predictive pressure drop models for membrane channels with non-woven and woven spacers, Desalination 376 (2015) 41–54.
[22] F. Ponzio, A. Tamburini, A. Cipollina, G. Micale, M. Ciofalo, Experimental and computational investigation of heat transfer in channels filled by woven spacers, Int. J. Heat Mass Transf. 104 (2017) 163–177.
[23] L. Gurreri, A. Tamburini, A. Cipollina, G. Micale, M. Ciofalo, Flow and mass transfer in spacer-filled channels for reverse electrodialysis: a CFD parametrical study, J. Membr. Sci. 497 (2016) 300–317.
[24] O. Kuroda, S. Takahashi, M. Nomura, Characteristics of flow and mass transfer rate in an electrodialyzer compartment including spacer, Desalination 46 (1983) 225–232.
[25] G. Kortum, Treatise on Electrochemistry, Elsevier Publishing Company, 1965.
[26] A. De Diego, A. Usobiaga, J.M. Madariaga, Critical comparison among equations derived from the Falkenhagen model to fit conductimetric data of concentrated electrolyte solutions, 446 (1998) 177–187.
[27] P. Długołęcki, P. Ogonowski, S.J. Metz, M. Saakes, K. Nijmeijer, M. Wessling, On the resistances of membrane, diffusion boundary layer and double layer in ion exchange membrane transport, J. Membr. Sci. 349 (1) (2010) 369–379.
[28] R.K. McGovern, A.M. Weiner, L. Sun, C.G. Chambers, S.M. Zubair, J.H. Lienhard V, On the cost of electrodialysis for the desalination of high salinity feeds, Appl. Energy 136 (December 2014) 649–661.
[29] R. Robinson, R. Stokes, Electrolyte Solutions, Butterworth & Co., 1970.
[30] R. Allgood, A. Gordon, The variation of the transference numbers of sodium chloride in aqueous solution with temperature, J. Chem. Phys. 10 (1942) 124–126.
[31] R. Stokes, The diffusion coefficients of eight uni-univalent electrolytes in aqueous solution at 25°, J. Am. Chem. Soc. 72 (5) (1950) 2243–2247.
[32] V. Geraldes, M.D. Afonso, Limiting current density in the electrodialysis of multiionic solutions, J. Membr. Sci. 360 (1) (2010) 499–508.
[33] A.R. Da Costa, A.G. Fane, D.E. Wiley, Spacer characterization and pressure drop modelling in spacer-filled channels for ultrafiltration, J. Membr. Sci. 87 (1994) 79–98.
[34] K.M. Chehayeb, J.H. Lienhard, Entropy generation analysis of electrodialysis Entropy generation analysis of electrodialysis, Desalination 413 (2017) 184–198.
[35] PCA GmbH, PC Cell ED 64 0 02 Technical Description 2016.
[36] PCA GmbH, PCA Ion Exchange Membranes: Technical Data Sheet 2016.
[37] GE Power & Water., Specification for Electrodialysis Ion Exchange Membranes 2010.
[38] D. Nwal Amang, S. Alexandrova, P. Schaetzel, The determination of diffusion coefficients of counter ion in an ion exchange membrane using electrical conductivity measurement, Electrochim. Acta 48 (18) (2003) 2563–2569.
[39] GE Power & Water, GE Aquamite EDR Systems, FS1360EN.
[40] Water Environment Federation American Water Works Association, American Public Health Association. Standard Methods for the Examination of Water and Wastewater, Washington DC, 1999.
[41] Bureau of Indian Standards, IS:3025 Indian Standard Methods of Sampling and Test for Water and Wastewater, Part 24, New Delhi, 1986.
[42] Central Pollution Control Board, Guide Manual: Waster and Wastewater Analysis, Delhi, (2011).
[43] D.F. Bender, Comparison of Methods for the Determination of Total Residual Chlorine in Various Sample Matrices, EPA-600/4-78-019, Cincinnati, Ohio, 1978.